Applied Surface Science 510 (2020) 145315

Contents lists available at ScienceDirect

Applied Surface Science

journal homepage: www.elsevier.com/locate/apsusc

Full Length Article

Triple VTe_2/graphene/VTe_2 heterostructures as perspective magnetic tunnel junctions

Lyudmila V. Begunovich[a,*], Artem V. Kuklin[a,b], Maxim A. Visotin[a,c], Alexander A. Kuzubov[1], Felix N. Tomilin[a,c], Anton S. Tarasov[a,c], Yuri G. Mikhalev[a], Pavel V. Avramov[d]

[a] Siberian Federal University, 79 Svobodny Av., Krasnoyarsk 660041, Russian Federation
[b] Department of Theoretical Chemistry and Biology, School of Engineering Sciences in Chemistry, Biotechnology and Health, Royal Institute of Technology, Stockholm SE-10691, Sweden
[c] Kirensky Institute of Physics SB RAS, 50-38 Akademgorodok, Krasnoyarsk 660036, Russian Federation
[d] Department of Chemistry, Kyungpook National University, 80 Daehakro, Bukgu, Daegu 41566, Republic of Korea

ARTICLE INFO

Keywords:
Magnetic tunnel junction
Vanadium ditelluride monolayer
Transition metal dichalcogenides
Graphene
Density functional theory

ABSTRACT

New perspective 1.4 nm thick spin-polarized triple heterostructures based on graphene sandwiched between two vanadium ditelluride monolayers (VTe_2/graphene/VTe_2) were studied using *ab initio* DFT technique. Both possible trigonal prismatic (*H*-VTe_2) and octahedral (*T*-VTe_2) VTe_2 phases were considered to design and study graphene-based heterostructures. It was shown that the interaction with graphene changes the electronic structure of 2D *T*-VTe_2 from metallic to half-metallic, making *T* phase perspective to be used for magnetic tunnel junctions. The electronic subsystem of graphene fragment is slightly hole doped. Calculated tunnel magnetoresistance ratio for the favorable heterostructure configuration estimated within the Julliere model is 220%, which opens a way to use VTe_2/graphene/VTe_2 as prospective magnetic tunnel junction in novel spintronic nanodevices based on tunnel magnetic resistance and spin transfer torque effects.

1. Introduction

Spintronics attracts ever-increasing scientific interest due to the possibility for further enhancement of modern electronic devices [1,2]. This can be achieved through complement or even replacement of the charge degree of freedom by electrons' spin for data transfer, processing and storage. The first spin devices that have found their application in electronics as disk read-and-write heads were the magnetic junctions based on giant magnetoresistance effect (GMR) [3]. A logical development of magnetoresistive devices and their manufacture technology was a demonstration of tunneling magnetoresistance (TMR) at room temperature in epitaxial magnetic tunnel junctions (MTJs) with MgO barrier fabricated by molecular beam epitaxial growth [4–6]. The TMR effect value more than 100% allows one to use such MTJs not only to create magnetic field sensors and reading heads of hard drives but also to make magnetoresistive random access memory (MRAM) [7]. The discovery of spin transfer torque effect (STT) [8] makes MTJs more attractive to produce different spintronic devices, including MRAM [9], radio-frequency sensors [10], microwave generators and even artificial neural networks [11].

Key advantages of MTJs-based devices are non-volatility, low power consumption, high processing speed, high integration density and metal–oxide–semiconductor technology compatibility. The most frequently used materials for MTJs fabrication are ferromagnetic metals and alloys like Fe and CoFeB, various Heusler alloys and dielectrics such as AlO_x and MgO [12]. At the same time, great progress has been achieved in two-dimensional (2D) materials synthesis and creation of spintronic devices based on monolayers [13,14]. Because of quantum nature and low dimensionality, applications of 2D materials add some advantages for novel electronic devices like flexibility [15], and extremely high scaling.

The layered structures like transition metal dichalcogenides (TMD) are the most attractive materials for monolayer synthesis. In such structures adjacent layers are coupled by weak van der Waals forces, thus it is possible to easily separate one layer from the rest of the crystal. The common methods of TMD monolayer fabrication are chemical vapor deposition (CVD) and mechanical exfoliation [16]. At the same time, the recent progress in synthesis allows one to fabricate a single layer directly from solution (liquid exfoliation methods) [17]. These methods produce the highest-quality samples [17–23] which can

* Corresponding author.
E-mail address: lyuda.illuzia@gmail.com (L.V. Begunovich).
[1] Deceased December 31, 2016.

https://doi.org/10.1016/j.apsusc.2020.145315
Received 30 August 2019; Received in revised form 12 December 2019; Accepted 7 January 2020
Available online 17 January 2020
0169-4332/

be successfully used in high-performance devices.

Among large TMD family, vanadium dichalcogenides VX_2 (X = S, Se, and Te) were predicted to be magnetic materials [24–31] as well as other vanadium-based materials [32–34]. Different *ab initio* approaches predict stability of both trigonal prismatic *H*- and octahedral *T*-phases of 2D VX_2 with *T*-VTe_2 and probably *H*-VSe_2 and *H*-VS_2 being energetically favorable [23,24,35–37]. According to various theoretical publications [23–28,31,38–42] 2D VX_2 can be metals, semimetals, ultra-narrow-band-gap semiconductors or semiconductors with ferromagnetic or non-magnetic ground states depending on composition, phase and *ab initio* approach. VSe_2 and VTe_2 are of special interest due to possible existence of room-temperature ferromagnetism [28,30].

Graphene, a single atomic carbon sheet, is very promising material for spintronic application [43]. Cobas *et al.* [44] demonstrated graphene as an insulator for transport perpendicular to the plane and effective tunnel barrier between two ferromagnetic metal NiFe and Co electrodes. Some TMD/graphene heterostructures were also successfully synthesized [45,46] creating an opportunity to construct new perspective magnetic junctions based on vanadium dichalcogenides.

In this paper, new ultrathin magnetic tunnel junctions based on vanadium ditelluride monolayers and graphene as a tunnel barrier were proposed and studied using density functional theory generalized gradient approximation (DFT-GGA) calculations. The atomic and electronic structures of *T*-VTe_2 were tested using hybrid functional and the atomic geometry, electronic structure and magnetic properties of two possible bilayer structures containing graphene and *T*- or *H*-VTe_2 single layer were studied to investigate the interactions between the 2D fragments. It was shown that interaction with graphene change the electronic structure of 2D *T*-VTe_2 from metallic to half-metallic state, making this phase perspective in spintronics. Several possible magnetic triple VTe_2/graphene/VTe_2 tunnel junctions were designed to search preferred configurations. It was found that in the framework of Julliere model, the theoretical TMR ratio for energetically favorable heterostructure is 220%.

2. Computational details

Calculations were carried out within the Perdew–Burke–Ernzerhof generalized gradient approximation (PBE) [47] implemented in the Vienna *ab-initio* simulation package (VASP) [48]. Empirical D2 correction of Grimme [49] was included to take into account weak van der Waals interactions in layered heterostructures. The electron-ion interactions were described by the projector augmented wave (PAW) method [50] and the plane-wave cutoff energy of 400 eV was applied. The criteria for the total energy minimization and interatomic forces were set to 10^{-4} eV and 10^{-2} eV $Å^{-1}$, respectively. To simulate 2D structures using Periodic Boundary Conditions (PBC), the periodic replicas were separated by a vacuum spacing of at least 20 Å along the *c* axis, which is perpendicular to the VTe_2 and graphene planes. The first Brillouin zone (1BZ) was sampled by 12 × 12 × 6 and 12 × 12 × 1 grids for bulk VTe_2 and VTe_2 monolayers and layered heterostructures, respectively using the Monkhorst–Pack scheme [51]. The non-collinear spin-polarized calculations were carried out to examine spin-orbital interactions in ferromagnetic *T*-VTe_2 monolayer and both *T*-VTe_2/graphene and *H*-VTe_2/graphene heterostructures. Band structure calculations were performed along the high symmetry *Γ(0,0,0)-M(1/2,0,0)-K(1/3,1/3,0)-Γ(0,0,0)* directions in 1BZ. In order to assess the adequacy of our PBE results the calculations of atomic structure and electronic properties of *T*-VTe_2 monolayer and atomic structure of *H*-VTe_2 monolayer were performed using both PBE and the screened-nonlocal-exchange Heyd-Scuseria-Ernzerhof (HSE06) functional [52]. The Visualization for Electronic and Structural Analysis (VESTA) software [53] was used for representation of atomic structures.

To determine the magnetic easy-axis and magnetocrystalline anisotropy energy (MAE), the total energies (*E*) of a structure with the spins of *V* atom constrained in [1 0 0], [0 1 0] and [0 0 1] directions were calculated using the PBE functional and spin–orbit coupling (SOC) under the energy convergence criteria of 10^{-7} eV. The out-of plane and in-plane MAE were calculated as $(E_{[0\ 0\ 1]} - E_{[1\ 0\ 0]})/n$ and $(E_{[1\ 0\ 0]} - E_{[0\ 1\ 0]})/n$, respectively, where *n* is a number of *V* atoms in a unit cell.

The all-electron one-center contribution of the SOC was described using Hamiltonian:

$$H_{SOC}^{\alpha\beta} = \frac{\hbar^2}{(2m_e c)^2}\left(\frac{1}{r} - \frac{V(r)}{2m_e c^2 r}\right)^{-2}\frac{dV(r)}{dr}\vec{\sigma}^{\alpha\beta}\bullet\vec{L}$$

where m_e is the mass of the electron, *c* is the speed of light in vacuum, $\hbar$ is the reduced Planck constant, $\vec{\sigma} = (\sigma_x, \sigma_y, \sigma_z)$ are the Pauli spin matrices, α and β are the spin-up and spin-down components of the two-component spinor wave functions, *r* is the sphere radius, $V(r)$ is the spherical part of the effective all-electron potential within the PAW sphere, $\vec{L} = \vec{r} \times \vec{p}$ is the angular moment operators, $\vec{p}$ is a momentum of the electron [54–56].

The interlayer binding energies (E_{bind}) were calculated using the following equation:

$$E_{bind} = E_{tot} - E_{gr} - mE_{VTe},$$

where E_{tot} is the total energy of a heterostructure, E_{gr} and E_{VTe} are energies of freestanding graphene and vanadium ditelluride fragments, respectively, and *m* is a number of vanadium ditelluride layers in a heterostructure.

To calculate the Fermi level spin polarizations of VTe_2 fragments the following equation was used:

$$P = \frac{\rho_\uparrow(\varepsilon_F) - \rho_\downarrow(\varepsilon_F)}{\rho_\uparrow(\varepsilon_F) + \rho_\downarrow(\varepsilon_F)},$$

where $\rho_\uparrow(\varepsilon_F)$ and $\rho_\downarrow(\varepsilon_F)$ are density of states of VTe_2 fragment at the Fermi level (ε_F) for electrons with spin-up (↑) and spin-down (↓).

The TMR ratio has been estimated within the Julliere model [57,58] for T = 0 K:

$$TMR = \frac{2P_{up}P_{down}}{1 - P_{up}P_{down}}\bullet 100\%,$$

where *P* is the Fermi level spin polarization of VTe_2 fragment, located above (*up*) and below (*down*) graphene fragment.

The unit cells of free-standing VTe_2 monolayers contain one *V* atom and two *Te* atoms, the unit cells of bilayer VTe_2/graphene heterostructures contain four *V* atoms, eight *Te* atoms and eighteen *C* atoms, the unit cells of triple VTe_2/graphene/VTe_2 heterostructures contain eight *V* atoms, sixteen *Te* atoms and eighteen *C* atoms. *C* s^2p^2, *V* s^2d^3, *Te* s^2p^4 valence electrons were used with pseudopotentials for carbon, vanadium and tellurium atoms, respectively.

3. Results and discussion

3.1. Atomic and electronic structure of free-standing T-VTe_2 and H-VTe_2 monolayers

The unit cells of 2D *H*- and *T*-VTe_2 phases and atomic numbering schemes are presented in Fig. 1. For the sake of comparison, the details of atomic and electronic structure of 2D *T*-VTe_2 and atomic structure of 2D *H*-VTe_2 at both HSE06 and PBE levels of theory were considered. Electronic structure and magnetic properties of *H*-VTe_2 monolayer were studied in details previously [26]. Taking into account the data discrepancy between reported magnetic properties (ferromagnetic or nonmagnetic) of *T*-VTe_2 monolayer [24,28,35] and the key requirement of ferromagnetic ordering of magnetic layers for MTJs, nonmagnetic, ferromagnetic, checkerboard and collinear antiferromagnetic states were studied to establish the ground state of the monolayer. Schematic views of magnetic configurations are presented at Fig. 2.

The PBE calculations demonstrate that the ferromagnetic configuration of *T*-VTe_2 monolayer is energetically preferable with the energy

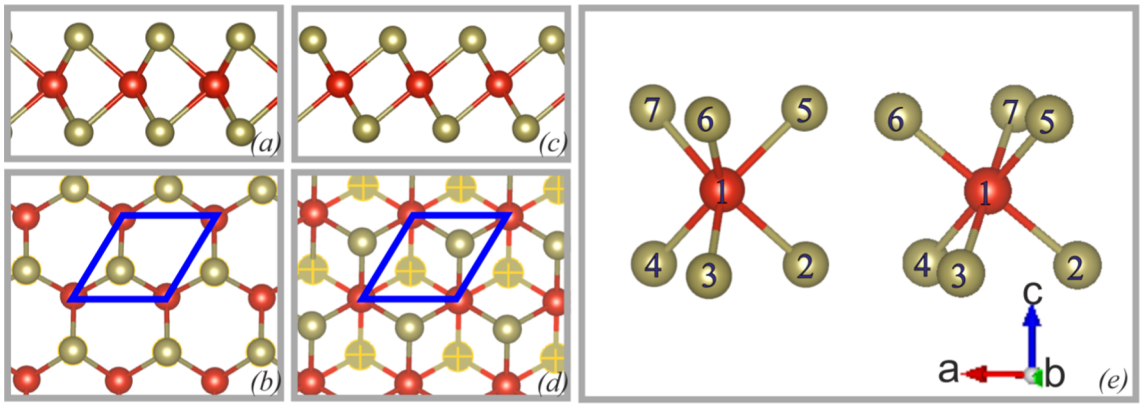

Fig. 1. Atomic structure of single-layer 2D VTe_2: side and top views of *H*-VTe_2 *(a, b)* and *T*-VTe_2 (*c, d*) monolayers. Trigonal prismatic (left) and octahedral (right) vanadium coordinations and the atomic numbering scheme (*e*). Hexagonal unit cells have been shown in blue. Red (olive) color corresponds to vanadium (tellurium) atoms. (For interpretation of the references to colour in this figure legend, the reader is referred to the web version of this article.)

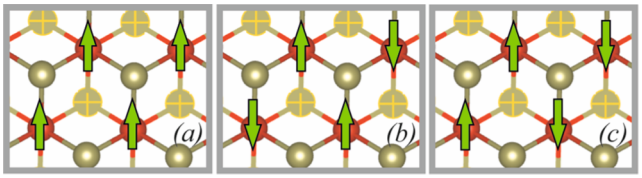

Fig. 2. Scheme of magnetic configurations of single-layer 2D *T*-VTe_2: ferromagnetic *(a)*, checkerboard antiferromagnetic *(b)*, and collinear antiferromagnetic *(c)* vanadium spin arrangements. Red (olive) color corresponds to vanadium (tellurium) atoms. (For interpretation of the references to colour in this figure legend, the reader is referred to the web version of this article.)

difference between ferromagnetic and nonmagnetic states being −0.024 eV per unit cell. The HSE06 functional makes this difference even larger (−0.623 eV), which is significantly greater the accuracy of DFT approach. There is no energy difference between checkerboard and collinear antiferromagnetic states. In comparison with both antiferromagnetic configurations, the ferromagnetic ordering is energetically favorable by −0.013 eV per unit cell at the PBE level of theory and by −0.036 eV at HSE06 one. The PBE functional reveals 0.979 μ_B magnetic moment on *V* atom of *T*-VTe_2 monolayer with small opposite magnetic moments (−0.065 μ_B) induced at *Te* atoms that is in a good agreement with [24]. In the case of *H*-VTe_2 monolayer, a number of theoretical investigations [24–26,35] revealed the ferromagnetic configuration as the ground state. Calculated out-of-plane MAE of *T*-VTe_2 monolayer is 0.763 meV, while the in-plane MAE is equal to 0. This implies that *T*-VTe_2 monolayer belongs to the category of *XY* magnets with easy *xy* plane of magnetization, that is in a good agreement with the results for *H*-VTe_2 monolayer [26]. MAEs of *H*- and *T*-VTe_2 monolayers are larger than MAEs for the bulk Fe and Ni (1.4 μeV/ion and 2.8 μeV/ion, respectively) [59]. The calculated structural parameters of both *H*- and *T*-VTe_2 monolayers within PBE and HSE06 levels of theory are listed in Table 1 and are in excellent agreement with previous theoretical results [24–26].

Table 1
Equilibrium structural parameters of ferromagnetic *H*- and *T*-VTe_2 monolayers: The lattice vectors (Å), *V-Te* bond length (Å) and thickness (Å).

Functional	Lattice vector ($\vec{a} = \vec{b}$), Å	Bond length *V-Te*, Å	Thickness, Å
H-VTe_2 monolayer			
PBE	3.58	2.71	3.51
HSE06	3.58	2.71	3.51
T-VTe_2 monolayer			
PBE	3.58	2.70	3.42
HSE06	3.60	2.72	3.46

The spin-polarized band structure along the high symmetry *Γ(0,0,0)-M(1/2,0,0)-K(1/3,1/3,0)-Γ(0,0,0)* directions in the Brillouin zone and total density of states (TDOS) of *T*-VTe_2 monolayer calculated within HSE06 and PBE functionals (Figs. 3 and 4) reveal a metallic behavior of *T*-VTe_2 as reported before [60]. The results show weak spin–orbit coupling (SOC) in *V* atom being of the order to −0.007 eV and more strong SOC in *Te* atoms (−0.209 eV). Due to the fact that the vanadium electron states dominate around the Fermi level, the electronic and magnetic properties remain close for both cases (with and without taking into account SOC), for this reason SOC are not taken into account in most of further calculations. This result is in a good agreement with results for 2D *H*-VX_2 (X = S, Se and Te) [26]. At PBE, PBE + SOC and HSE06 levels of theory, the 2D *T*-VTe_2 phase is energetically favorable with relative energies of 2D *H*-VTe_2 phase equal to 0.055, 0.049 and 0.213 eV, respectively, which is in a good agreement with Refs. [24,35]. Taking into consideration the large number of atoms in the unit cells of heterostructures and good agreement of PBE and HSE06 results further calculations were performed at PBE level of theory. Although the *T* configuration is energetically preferable, creation of the heterostructures with graphene can affect the structural stability, so both *T* and *H* phases were considered to design the heterostructures.

3.2. Bilayer *T*-VTe_2/graphene and *H*-VTe_2/graphene heterostructures

The bilayer heterostructures, were designed by deposition of graphene on top of *T*- or *H*-VTe_2 monolayers (let's denote them for simplicity as *T*/graphene and *H*/graphene, respectively) in order to investigate the interactions between the fragments (Fig. 5(a) and (b)). As the full relaxed lattice constant of isolated graphene (a = 2.46 Å) is about 31% smaller than that of isolated VTe_2 monolayer (a = 3.58 Å), we constructed the bilayer heterostructures, consisting of 2 × 2 VTe_2 (the translation vector is equal to 7.16 Å) and 3 × 3 graphene (the translation vector is equal to 7.39 Å) unit cells. Consequently, the remaining lattice mismatch between graphene and VTe_2 fragments of about 3.21% is reasonably small. We increased lattice parameter of VTe_2 layer in order to fit graphene lattice parameter, because the PBC were used to calculate the heterostructures.

In the case of *H*/graphene, one non-equivalent *C* atom is located directly above *V* atom and its fractional coordinates along *a* and *b* axis are equal to 0. Another non-equivalent *C* atom is set to sit directly on top of inner *Te* atom (a = 0.(6), b = 0.(3)). In *T*/graphene three non-equivalent *C* atoms are on top of *V* (a = 0, b = 0), outer *Te* (a = 0.(3), b = 0.(6)) and inner *Te* (a = 0.(6), b = 0.(3)) atoms, respectively. In this work, *Te* atoms located near graphene sheet are called "inner *Te* atoms" and *Te* atoms located on the opposite side of VTe_2 fragment are

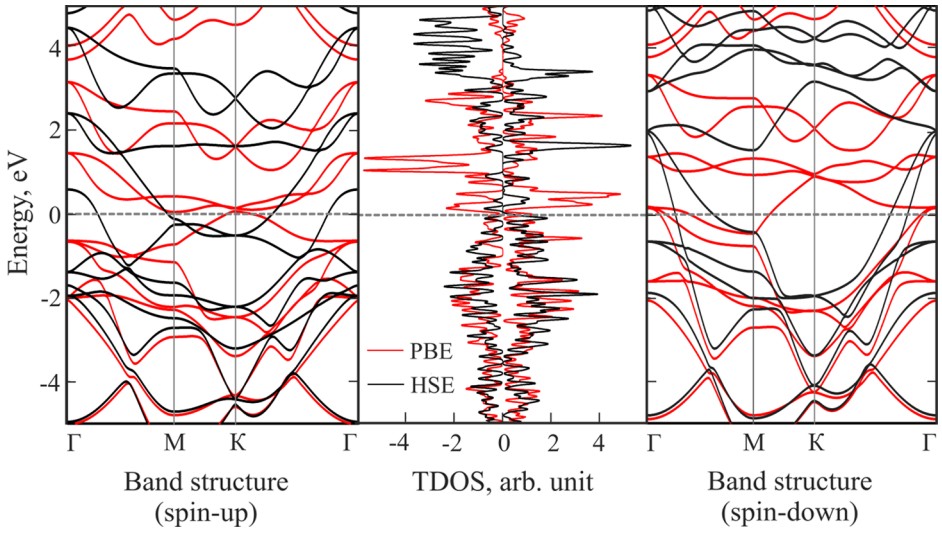

Fig. 3. Band structure and total density of states (TDOS) of ferromagnetic 2D *T*-VTe_2 unit cell at PBE (red) and HSE06 (black) levels of theory. The energy zero corresponds to the Fermi level. The left and right pictures correspond spin-up and spin-down densities, respectively. Spin-up and spin-down TDOS channels are demonstrated at positive and negative panels, respectively. (For interpretation of the references to colour in this figure legend, the reader is referred to the web version of this article.)

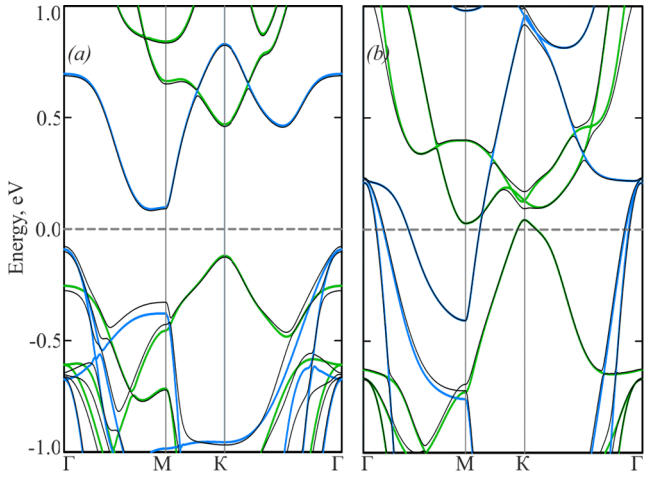

Fig. 4. PBE band structures of ferromagnetic 2D *H*-VTe_2 (*a*) and *T*-VTe_2 (*b*) unit cells with (black lines) and without (green and blue lines) spin orbit coupling. The green and blue lines correspond to spin-up and spin-down channels, respectively. The energy zero corresponds to the Fermi level. (For interpretation of the references to colour in this figure legend, the reader is referred to the web version of this article.)

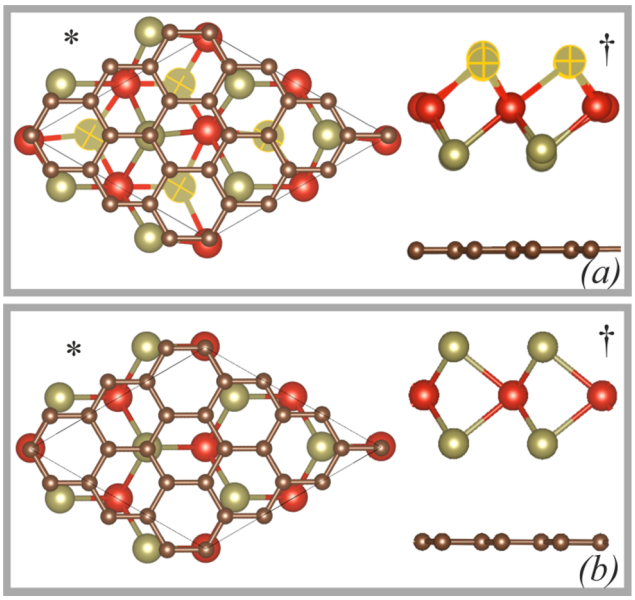

Fig. 5. Top (*) and side (†) views of bilayer *T*/graphene (*a*) and *H*/graphene (*b*) heterostructures. Hexagonal unit cells of heterostructures are shown in black. *(a)* Three non-equivalent *C* atoms of graphene fragment of *T*/graphene are on the top of *V* ($a = 0, b = 0$), outer *Te* ($a = 0.(3), b = 0.(6)$) and inner *Te* (a = 0.(6), b = 0.(3)) atoms of *T*-VTe_2 fragment, respectively. (*b*) Two non-equivalent *C* atoms of graphene fragment of *H*/graphene is located directly above *V* ($a = 0, b = 0$) and *Te* ($a = 0.(6), b = 0.(3)$) atoms of *H*-VTe_2 fragment. The figures show four *C* atoms located above the *V* atoms, three of which are translations of the first one. For *T*/graphene, the outer *Te* atoms are highlighted in yellow. *Te* atoms located near graphene sheet are denoted as "inner *Te* atoms" and *Te* atoms located on the opposite side of VTe_2 fragment are denoted as "outer *Te* atoms". *a* and *b* are fractional coordinates. Red, olive and brown colors correspond to vanadium, tellurium and carbon atoms, respectively. (For interpretation of the references to colour in this figure legend, the reader is referred to the web version of this article.)

called "outer *Te* atoms". Non-equivalent atoms are meant atoms that lie in a unit cell of heterostructure (the basis of a unit cell). The optimized structural parameters of localized *T*/graphene and *H*/graphene are presented in Tables 2 and 3.

The relaxed translation vector of *T*/graphene is equal to 7.36 Å (Table 2). In this bilayer heterostructure, the *T*-VTe_2 fragment is expanded by 2.79% as compared to the free-standing monolayer (from 7.16 to 7.36 Å), while graphene fragment is compressed by 0.41% (from 7.39 to 7.36 Å). All *V* and *Te* atoms located directly under *C* atoms are shifted towards nearest carbon atoms, resulting in distortion of the *T*-VTe_2 fragment with unequal *V-Te* bond lengths and *Te-V-Te* angles (Tables 3). The nearest outer and inner *Te* atoms are located 0.22 and 0.19 Å closer to graphene plane compared to others outer and inner *Te* atoms, respectively. The *V* atom located directly under *C* atom is located 0.07 Å closer to graphene plane then other *V* atoms, resulting in alteration of angles and bond lengths. Thus, three of the *V-Te* bond lengths of each *V* atom are longer while the other three ones are shorter (Tables 3).

As a result of the structural distortions, the magnetic moments of *V* and *Te* atoms in *T*/graphene are larger in absolute values then in free-standing *T*-VTe_2 monolayer. The magnetic moments of *Te* atoms depend on bond lengths with *V* atoms: an atom with longer bond lengths has smaller magnetic moment. Magnetic moment on the outer *Te* atom located directly under *C* atom is $-0.083\ \mu_B$ (*V-Te* bond lengths equal to 2.77 Å), while other outer *Te* atoms demonstrate $-0.102\ \mu_B$ (*V-Te* bond lengths equal to 2.67 and 2.76 Å). The inner *Te* atoms possess magnetic moment of $-0.094\ \mu_B$. (*V-Te* bond lengths equal to 2.69 and 2.77 Å), The *V* atom located directly under *C* atom has the lowest magnetic moment of 1.195 μ_B compared to other vanadium atoms (1.480 μ_B).

Table 2
Structural and magnetic parameters of localized bi- and triple-layer heterostructures at PBE level of theory. *P* and *AP* denote parallel and antiparallel spin ordering of adjacent ferromagnetic vanadium ditelluride layers in triple-layer heterostructures. The interlayer distance is the minimal distance between graphene sheet and inner *Te* ions of VTe_2 fragment. Asterisk (*) indicates distance between graphene and the second VTe_2 fragment when they are different. Relative energy is the energy difference between total energy of bi- or triple-layer heterostructures and the total energy of energetically favorable bi- or triple-layer heterostructure. All distances are in Å, all energies are in eV.

Heterostructure	Magnetization alignment: parallel (*P*), antiparallel (*AP*)	Translation vector $a = b$, Å	Interlayer distance, Å	Heterostructure thickness, Å	Relative energy, eV	Interlayer binding energy per cell E_{bind}, eV	ΔE (P-AP), eV
H/graphene	–	7.35	3.55	7.00	0.386	−0.660	–
T/graphene	–	7.36	3.42	6.71	0.000	−0.991	–
*H*_gr_*H*_[*AA*]	*P*	7.33	3.51	13.93	0.743	−1.471	0.001
	AP	7.33	3.51	13.93	0.742	−1.472	
*H*_gr_*H*_[*AB*]	*P*	7.33	3.51/3.54*	13.95	0.733	−1.482	0.000
	AP	7.33	3.51/3.54*	13.95	0.733	−1.482	
*T*_gr_*T*_[*AA'*]	*P*	7.36	3.49	13.73	0.000	−2.104	0.000
	AP	7.36	3.49	13.73	0.000	−2.104	
*T*_gr_*T*_[*AA*]	*P*	7.35	3.39/3.42*	13.67	0.002	−2.103	−0.001
	AP	7.35	3.39/3.42*	13.67	0.003	−2.101	
*T*_gr_*H*_[*AA*]	*P*	7.34	3.46/3.52*	14.00	0.377	−1.782	0.002
	AP	7.34	3.46/3.52*	14.00	0.379	−1.780	
*T*_gr_*H*_[*AB'*]	*P*	7.34	3.46/3.51*	14.00	0.372	−1.787	−0.001
	AP	7.34	3.46/3.51*	14.00	0.373	−1.786	

Table 3
V-Te bond lengths and *Te-V-Te* angles of bilayer heterostructures at PBE level of theory. The atomic numbering scheme is shown in Fig. 1(e). Asterisk (*) indicates values for *V* located at $a = 0$ and $b = 0$. All distances are in Å, all angles are in degrees.

Structure	Structural parameters			
	Bond	Bond length, Å	Angle	Angle value
H/graphene	2-1	2.73	2-1-5	78°
	1-6		3-1-6	
	3-1		4-1-7	
	1-7		2-1-3	84°
	4-1		2-1-4	
	1-5		3-1-4	
			5-1-6	
			5-1-7	
			6-1-7	
T/graphene	2-1	2.76 / 2.76*	2-1-6	171° / 177°*
	1-6	2.69 / 2.68*	3-1-7	169° / 177°*
	3-1	2.76 / 2.76*	4-1-5	171° / 177°*
	1-7	2.69 / 2.68*	2-1-3	83° / 88°*
	4-1	2.67 / 2.76*	2-1-4	86° / 88°*
	1-5	2.77 / 2.68*	2-1-5	86° / 95°*
			2-1-7	94° / 95°*
			6-1-3	94° / 94°*
			6-1-4	102° / 94°*
			6-1-5	85° / 83°*
			6-1-7	87° / 83°*

The total magnetic moment of the *T*/graphene heterostructure increases by 1.5 times in comparison to the freestanding *T*-VTe_2 monolayer and is equal to 4.799 μ_B.

The translation vector of relaxed *H*/graphene is equal to 7.35 Å (Table 2). The *H*-VTe_2 fragment is expanded by 2.65% (from 7.16 to 7.35 Å) and graphene fragment is compressed by 0.54% (from 7.39 to 7.35 Å) as compared to the free-standing monolayers. The *V-Te* bonds in *H*-VTe_2 fragment are slightly longer then in free-standing monolayer (Tables 3) with the total magnetic moment of *H*-VTe_2 increased by ~ 6% up to 4.130 μ_B. The magnetic moments on *V*, inner and outer *Te* atoms are 1.156, −0.092 and −0.094 μ_B, respectively.

The interlayer distances between graphene sheet and VTe_2 fragment of both bilayer heterostructures are 3.42 Å (Table 2) that indicates van der Waals interactions between the fragments. The graphene fragments in both heterostructures are slightly uneven with maximum distances between carbon positions along *c* axis 0.04 Å (*C*—*C* bond length 1.41 Å) and 0.06 Å (*C*—*C* bond length 1.42 Å) for *H*/graphene and *T*/graphene, respectively.

To compare the energetic stability of the bilayers, the interlayer binding energies (E_{bind}) were calculated, with correspondent values of −0.660 and −0.991 eV for *H*/graphene and *T*/graphene, respectively (Table 2). Negative binding energies for both heterostructures reveal that their fabrication is energetically feasible. The *T*/graphene heterostructure is energetically favorable with relative energy of *H*/graphene in respect to *T*/graphene equal to 0.386 eV.

The *H*-VTe_2 fragment of *H*/graphene as well as free-standing *H*-VTe_2 monolayer has easy *xy* plane of magnetization. In contrast to free-standing *T*-VTe_2 monolayer, due to the structure distortions, the *T*-VTe_2 fragment of *T*/graphene has magnetic easy axis along *x* direction with corresponding values of in-plane and out-of-plane MAE equal to −0.013 and 0.520 meV, respectively.

The structural changes are accompanied by changes in the electronic structure. At the PBE level of theory the calculated density of states (DOS) of *T*/graphene (Fig. 6) reveal significant changes of electronic structure of *T*-VTe_2 fragment under the influence of graphene π system. Fig. 6(a) clearly demonstrate significant redistribution of *T*-VTe_2 electronic densities in the vicinity of the Fermi level. It leads to the absence of spin-up states in the energy range from −0.095 to 0.226 eV (the Fermi level corresponds to zero energy) and increasing these states localized in −0.324 −0.095 eV range. Spin-down density of states is increased at the Fermi level. Hence VTe_2 fragment demonstrates 100% spin-polarized half-metallicity. In the case of *H*-VTe_2 fragment the electron density are shifted to lower energies (Fig. 6(*b*)), namely vacant spin-up and spin-down states are shifted to Fermi level by 0.135 and 0.180 eV, respectively, and occupied spin-up and spin-down states are shifted by 0.290 and 0.320 eV, respectively, to lower energies. Compared with the DOS of pristine graphene, the partial DOSs of graphene fragments are perturbed (Fig. 6*(c, d)*) almost similar to the previously described physiosorped graphene-based heterostructures [61] with small amounts of spin-down and spin-up states at the Fermi level (Fig. 6*(c, d)*).

For the sake of comparison the electronic structure of freestanding *T*-VTe_2 and *H*-VTe_2 monolayers at tensile strain of 2.79% (corresponds to *T*/graphene heterostructure) and 2.65% (corresponds to *H*/graphene heterostructure) was considered as well. Strained *T*-VTe_2 monolayer demonstrates metallic behavior (Fig. 7(*a*)), whereas *T*-VTe_2 fragment possesses half-metallic properties (Fig. 8(*a*)). In this case the strain leads to a certain increase in the density of states at the Fermi level,

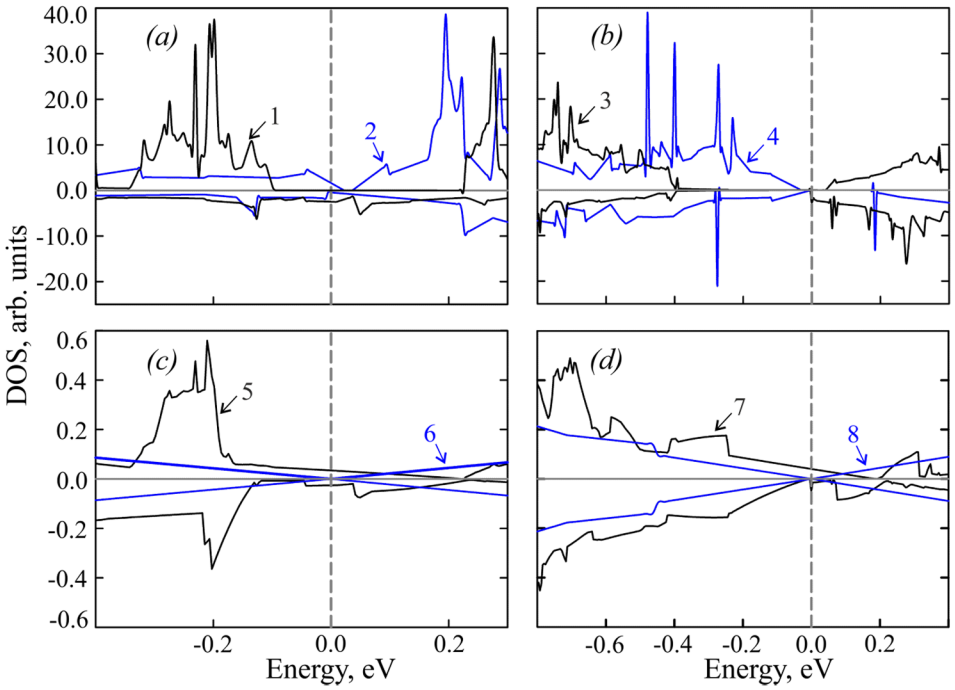

Fig. 6. Spin-polarized densities of states (DOSs) of supercells of free-standing monolayers and fragments of bilayer heterostructures at the PBE level of theory. In detail, partial DOSes of *T*-VTe_2 fragment from *T*/graphene (*a*, solid black line 1), total DOSes of free-standing *T*-VTe_2 monolayer (*a*, solid blue line 2), partial DOSes of *H*-VTe_2 fragment from *H*/graphene (*b*, solid black line 3), total DOSes of free-standing *H*-VTe_2 monolayer (*b*, solid blue line 4), partial DOSes of graphene fragment from *T*/graphene (*c*, solid black line 5), total DOSes of free-standing graphene (*c*, solid blue line 6 and *d*, solid blue line 8), partial DOSes of graphene fragment from *H*/graphene (*d*, solid black line 7). The Fermi level corresponds to zero energy. Spin-up and spin-down DOS channels are demonstrated at positive and negative panels, respectively. (For interpretation of the references to colour in this figure legend, the reader is referred to the web version of this article.)

enhancing the metallic character of the *T*-VTe_2 monolayer (Fig. 7(*a*)). In the case of strained *H*-VTe_2 monolayer (Fig. 7(*b*)), the shift of the vacant states to higher energies is observed, while in the case of *H*-VTe_2 fragment (Fig. 8(b)) the shift of valence and vacant states to lower energies takes place. Thus, the results demonstrate that in comparison with tensile strain, graphene layer plays a leading role in the formation of the electronic properties of VTe_2 fragments. It is the interaction with graphene that leads to such a specific structure of *T*-VTe_2, which allows the half-metallic state to be realized. The DOSs of graphene compressed up to 0.41 and 0.54%, which corresponds to graphene compression in bilayer heterostructures, just coincide to the DOS of pristine graphene. Hence, the electronic structure changes of graphene fragment are caused by interactions with VTe_2 fragments.

The band structure of *T*/graphene calculated at PBE level of theory is shown in Fig. 9(*a*). The top spin-down valence band and bottom spin-down conductivity band of *T*-VTe_2 electronic subsystem of T/graphene cross the Fermi level in *Γ*-*M* and *M* − *K* intervals, respectively, whereas spin-up states exhibit indirect band gap of ~0.3 eV with the valence-band maximum at *M* point and conduction-band minimum at *K* point, confirming half-metallicity of *T*-VTe_2 fragment in the *T*/graphene.

The *H*-VTe_2 electronic subsystem of *H*/graphene demonstrates semiconducting properties (Fig. 9(*b*)). The band gap of *H*-VTe_2 electronic subsystem is increased up to 0.33 eV as compared to free-standing *H*-VTe_2 monolayer (0.18 eV). The band structure of *H*/graphene calculated using PBE with SOC demonstrates the energy splitting between *V* bands in the *Γ*-*M* direction. Splitting attains its maximum at *M* point and vanishes at *Γ* point. Maximum splitting near the Fermi level in valence and conduction bands are equal to 0.052 and 0.089 eV, respectively.

To identify the reasons of energy splitting between *V* bands in *H*/graphene and the reasons of absence such splitting in *T*/graphene the influence of band folding effect, SOC and magnetic symmetry of structures on the band structures of 2D VTe_2 was studied. The results reveal no energy splitting in the electronic structures of *T*- and *H*-VTe_2 unit cells (Fig. 4) as well as in the electronic structure of 2 × 2 super cell of *T*-VTe_2 (Fig. 10). In the case of 2 × 2 super cell of *H*-VTe_2 the splitting is observed only in band structure calculated with taking into account SOC (Fig. 10). Observed energy splitting is similar to the splitting in *H*/graphene. The intervals in the first Brillouin zone of primitive cell, which are mapped by translation symmetry into the *Γ*–*M* interval of the first Brillouin zone of super cell, are highlighted in red (Fig. 10(*c*)). Actually the time reversal symmetry is absent in VTe_2 layer due to presence of magnetization in these structures, lying in plane along the *X* axis. Highlighted intervals are equivalent in energy and the bands are degenerate when SOC is not considered in the calculations, because of the mirror plane symmetry (perpendicular to *y* direction) contained in both *T*-VTe_2 and *H*-VTe_2 structures. When the SOC is included, the Hamiltonian is no longer invariant under that mirror plane transformations. However, the magnetic space group of *T*-VTe_2 (OG 12.1.66) contains C_{2y}' element of rotation with time reversal, which connects *k*-points (x y z) and (x –y z) and preserves the spin component along the magnetization axis. Therefore, no splitting has been found in

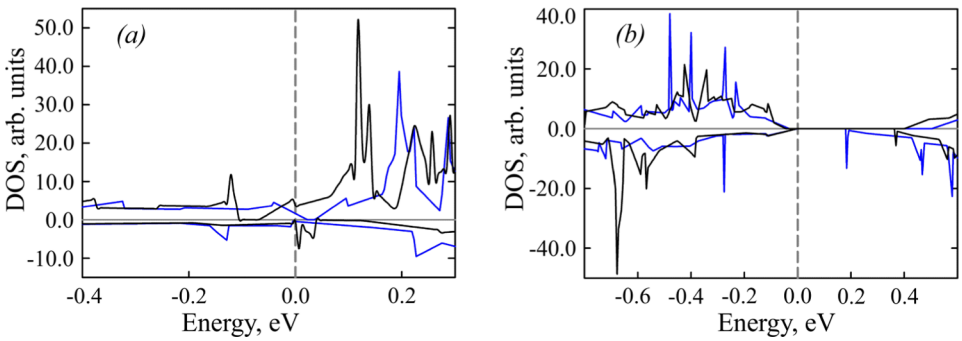

Fig.7. PBE density of states of 2 × 2 × 1 supercells of freestanding *T*- and *H*-VTe_2 monolayers (blue lines in (*a*) and (*b*), respectively), of 2 × 2 × 1 supercell of *T*-VTe_2 monolayer at tensile strain of 2.65% (black lines in (*a*)) and of 2 × 2 × 1 supercell of *H*-VTe_2 monolayer at tensile strain of 2.79% (black lines in (*b*)). The energy zero corresponds to the Fermi level. Spin-up and spin-down channels are demonstrated at positive and negative panels, respectively. (For interpretation of the references to colour in this figure legend, the reader is referred to the web version of this article.)

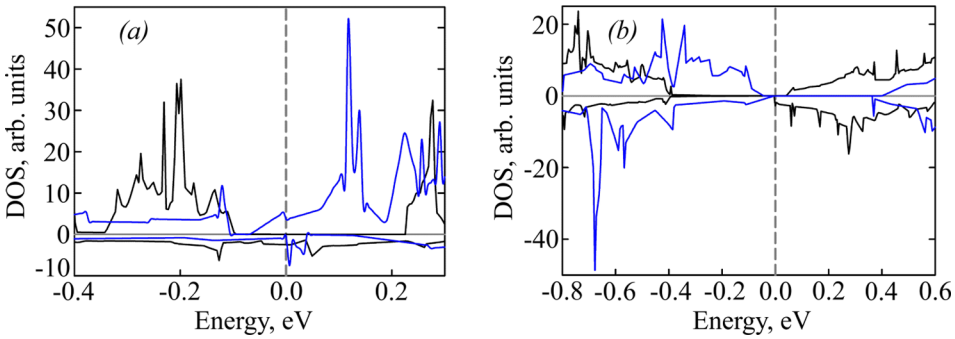

Fig. 8. PBE partial density of states of *T*- and *H*-VTe_2 fragments (black lines in (*a*) and (*b*), respectively) and density of states of 2 × 2 × 1 supercell of freestanding ferromagnetic VTe_2 monolayer at tensile strain of 2.65% for *T* configuration (blue lines in (*a*)) and 2.79% for *H* configuration (blue lines in (*b*)). The energy zero corresponds to the Fermi level. Spin-up and spin-down channels are demonstrated at positive and negative panels, respectively. (For interpretation of the references to colour in this figure legend, the reader is referred to the web version of this article.)

band structure of 2 × 2 super cell of *T*-VTe_2 calculated with SOC. On the other hand, the magnetic space groups of *H*-VTe_2 (OG 38.3.267) do not contain analogous symmetry operations and the energy splitting of the bands is observed. Thus observed energy splitting between bands in *H*/graphene is caused by band folding effect and the reduction of symmetry. In general, SOC decreases band gap of *H*-VTe_2 monolayer more than twice (from 0.180 to 0.072 eV).

In both bilayer heterostructures the Dirac cone of graphene electronic subsystem presents at *Γ* point (Fig. 9) due to the band folding effect. In detail, the unit cells of heterostructures have nine primitive graphene cells, thus the new Brillouin zone is one-ninth of the original one. The k points of the initial Brillouin zone are re-mapped into the new zone by projection and *K* and *K'* symmetry points are projected on *Γ* point with mapping the cones to it (Fig. 11). The spin degeneracy at the Dirac point is lifted in all band structures calculated with and without SOC (inserted fragments in Fig. 9). The spin splitting values are in the range from 0.006 to 0.015 eV for *T*/graphene and from 0.016 to 0.030 eV for *H*/graphene. Following Ref [62], the lift of inversion symmetry can exhibit Bychkov-Rashba spin-orbit coupling (BR SOC) [63], which causes spin splitting of the bands [64,65]. Thus at the first stage the possibility of Bychkov-Rashba splitting of the Dirac cones was considered. The Bychkov-Rashba model Hamiltonian has the form

$$H_R = \alpha(\vec{\sigma} \times \vec{k})\cdot\vec{\nu}$$

where $\vec{\sigma}$ are Pauli matrices, $\vec{\nu}$ is a unit vector perpendicular to the heterostructure surface, α is the Bychkov-Rashba parameter, and $\vec{k}$ is a wave vector

$$\vec{p} = \hbar\vec{k}$$

where $\vec{p}$ is a quasimomentum and $\hbar$ is the reduced Planck constant. In BR systems the spin direction is perpendicular to the direction of the wave vector, and the resulting vector of the cross product is codirectional to $\vec{\nu}$. Hence the spin direction at $-\vec{k}$ is opposite to the spin direction at $\vec{k}$. Let's consider the direction of the spins at the Dirac cones in the intervals *-M(-1/2,0,0) – Γ(0,0,0) – M(1/2,0,0)* at the PBE level of theory taking into account SOC. For BR mechanism, the electron spins of the Dirac cones at *-M* point must be opposite to the spins at *M* point and directed opposite *y* axis (so, spins at *M* point are alongside *y*). The results of calculations show that the spins of half of bands are parallel to *z* axis and spins of other half of bands are antiparallel to *z* axis at *-M* and *M* points, respectively. It directly indicates that the spin splitting of the Dirac cone is not caused by the Bychkov-Rashba effect. This result is in a good agreement with [66], where the authors could not find the BR SOC in heterostructures based on graphene and ferromagnetic substrates such as graphene/Ni (1 1 1) and graphene/Co (0001).

The spin splitting of the Dirac cone in the band structures without SOC (Fig. 9) indicates that SOC does not play a key role in splitting. To identify the reasons of the splitting under study, the influence of the deformation of graphene, of the substrate magnetic field and of the overlapping between the wave functions of *C*-p_z states and of tellurium spin-polarized states on the Dirac cone were studied. For this purpose, band structures were calculated without SOC for graphene fragments from heterostructures, for heterostructures with a non-magnetic VTe_2 layer and for heterostructures with a ferromagnetic VTe_2 layer located further from the graphene fragment by 1 Å as compared to the equilibrium configurations. The results of calculations show that the deformation of graphene in considered heterostructures is too small to change the electronic structure of graphene and the spin degeneracy at the Dirac point is kept intact. In non-magnetic heterostructures, the Dirac cone is also doubly degenerated and is located ~0.1 eV above the

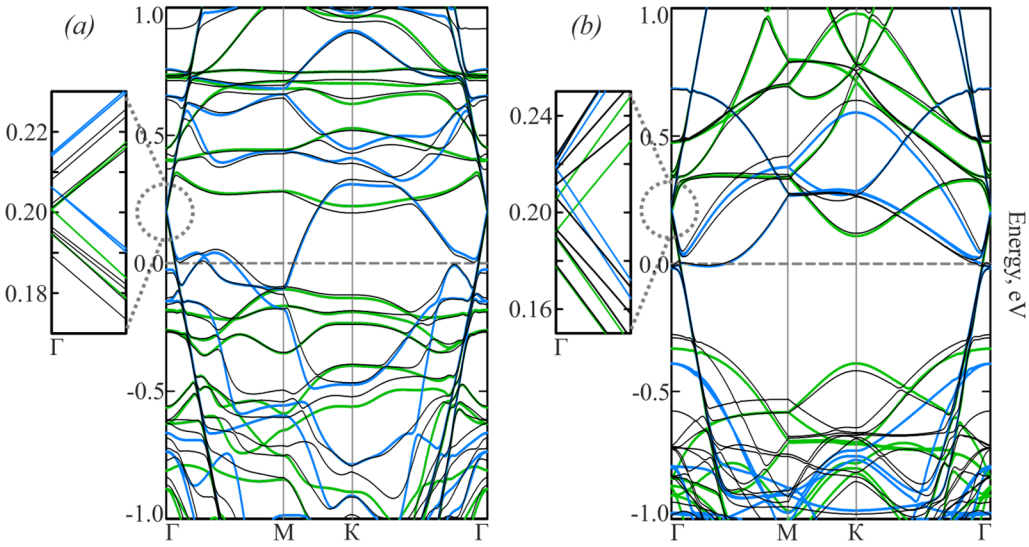

Fig. 9. Spin-resolved PBE band structures of *T*/graphene (left) and *H*/graphene (right) heterostructures calculated with (black lines) and without (green and blue lines) spin orbit coupling. The green and blue lines correspond to spin-up and spin-down channels, respectively. The energy zero corresponds to the Fermi level. Inserted fragments demonstrate splitting of graphene Dirac cones in the vicinity of *Γ* point. (For interpretation of the references to colour in this figure legend, the reader is referred to the web version of this article.)

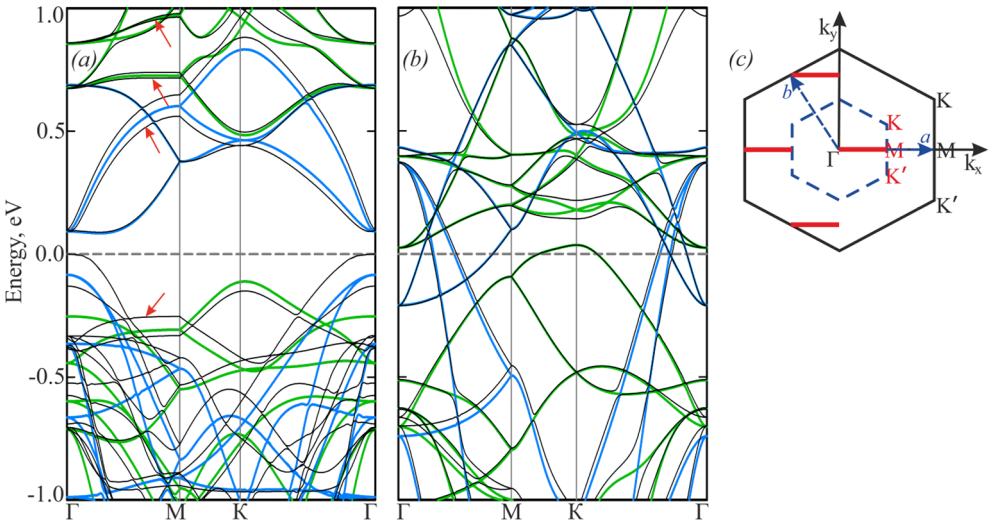

Fig. 10. Spin-resolved PBE band structure of freestanding 2D *H*-VTe_2 (a) and *T*-VTe_2 (b) 2 × 2 super cells calculated with (black lines) and without (green and blue lines) spin orbit coupling. The green and blue lines correspond to spin-up and spin-down channels, respectively. The energy zero corresponds to the Fermi level. (c) Schematic representation of band folding in the first Brillouin zone of 2D 2 × 2 VTe_2 supercell for *Γ-M* direction. Dashed blue and solid black lines indicate the first Brillouin zones of 2 × 2 supercell and primitive cell of VTe_2, respectively. Black (red) *K*, *K'*, *Γ* and *M* are high-symmetry points in primitive cell (supercell) Brillouin zone. *a* and *b* is primitive vectors of 2 × 2 VTe_2 monolayer in reciprocal space. Red lines indicate directions of primitive cell Brillouin zone that fold to the *Γ-M* direction of supercell Brillouin zone. Red arrows (a) show bands, which became energetically nonequivalent when SOC is included. (For interpretation of the references to colour in this figure legend, the reader is referred to the web version of this article.)

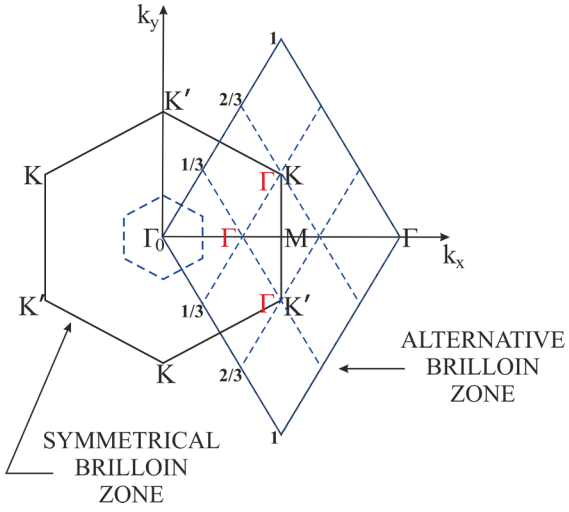

Fig. 11. Schematic representation of *K* and *K'* Dirac points folding to the *Γ* point in the first Brillouin zone of 3 × 3 graphene supercell. Blue and black lines indicate Brillouin zones of 3 × 3 supercell and primitive cell of graphene, respectively. Black *K*, *K'*, *Γ* and *M* are high-symmetry points in primitive cell Brillouin zone. Red *Γ* letters indicate the translation of the *Γ*point of supercell inside of first Brillouin zone of primitive cell. (For interpretation of the references to colour in this figure legend, the reader is referred to the web version of this article.)

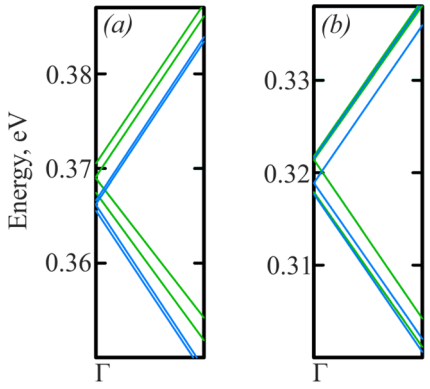

Fig. 12. The spin splitting of the Dirac cone at the PBE level of theory for *H*/graphene (a) and *T*/graphene (b) heterostructures with a ferromagnetic VTe_2 layer located further from the graphene fragment by 1 Å as compared to the equilibrium configuration. The green and blue lines correspond to spin-up and spin-down channels, respectively. The energy zero corresponds to the Fermi level. (For interpretation of the references to colour in this figure legend, the reader is referred to the web version of this article.)

Fermi level. Thus, it can be concluded that the magnetic substrate plays a leading role in spin splitting of the Dirac cone. In the case of a magnetic substrate that is 1 Å distant from the equilibrium position, another splitting is observed (Fig. 12). That means that spin splitting of the Dirac cone in bilayer heterostructures is caused not only by the magnetic field of the substrate, but also by the overlapping between the wave functions of *C*-p_z states $\Psi_i(i)$ and of spin-polarized states of tellurium atoms $\Psi_j(j)$, which leads to exchange interactions to satisfy the Pauli exclusion principle. *i* and *j* electrons with the same spin direction cannot be located in the overlap region, while *i* and *j* electrons with the opposite spin directions can be located at both Ψ_i and Ψ_j states (exchange interactions). As a result the cones with different spin directions become different in energy. SOC itself does not change the nature of the splitting, just introducing some small energy corrections to the bands. So, one can conclude that the spin splitting of the Dirac cones observed in *T*/graphene and H/graphene heterostructures is the exchange-mediated spin splitting. The results are in a good agreement with [65], where the authors revealed the exchange splitting of the Dirac cone of graphene with Ni adatoms on its surface.

In both heterostructures the charge transfer from graphene to vanadium ditelluride fragment (Fig. 13(*a*) and (*b*)) shifts the Fermi level below the Dirac point up to ~0.2 eV (Fig. 9) causing hole doping of graphene fragment. The charge transfer is defined as the difference in charge densities between bilayer heterostructure and superposition of electronic densities of free-standing fragments, located at the same positions as in the heterostructure. Blue and yellow colors in Fig. 13(*a*) and (*b*) represent electron-excess and electron-deficient areas, respectively. One can see that the negative charge is localized at inner tellurium atoms (blue areas in Fig. 13(*a*) and (*b*)), whereas the positive charge density is located at graphene sheet (yellow areas).

The calculated electron localization functions (ELF) [67] (Fig. 13(*c*) and (*d*)) reveal electron density localized mostly at *Te* atoms and a top the center of *C*—*C* bonds without electron gas localized in the interlayer region (ELF value is about 0), so the charge redistribution cannot be assigned for creation of covalent bonds between carbon atoms and *Te* atoms.

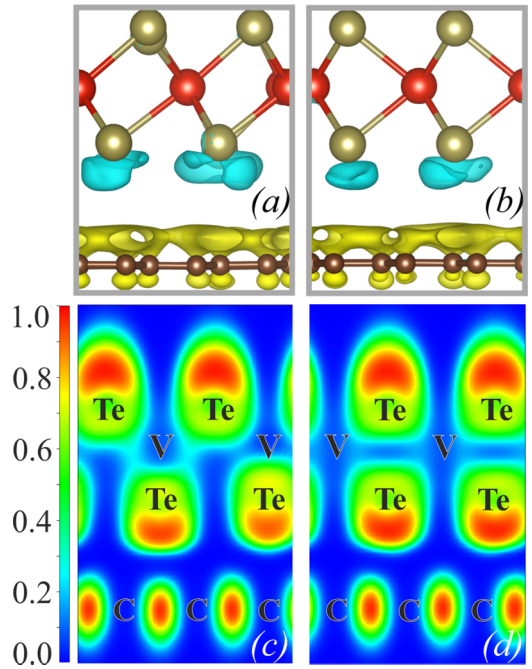

Fig. 13. Charge density differences and the electron localization functions of *T*/graphene (*a, c*) and *H*/graphene (*b, d*) at the PBE level of theory. *(a, b)* Charge density difference of *T*/graphene and *H*/graphene, respectively. The charge density difference is calculated as the difference between the total charge density of heterostructure and superposition of total charge densities of its fragments located exactly at the positions of corresponding fragments. Blue and yellow areas indicate electron-excess and electron-deficient regions, respectively. Red, olive and brown colors correspond to vanadium, tellurium and carbon atoms, respectively. Isosurface levels are (*a*): $1.3 \cdot 10^{-3}$ eÅ^{-3} and (b): $1.8 \cdot 10^{-3}$ eÅ^{-3} (*c, d*). Side view of the electron localization function renormalized to values between 0.0 and 1.0. The value of 1.0 characterizes the totally localized electrons and the value of 0.0 corresponds to the electrons with almost no localization. (For interpretation of the references to colour in this figure legend, the reader is referred to the web version of this article.)

3.3. Structure and electronic properties of H-VTe_2/graphene/H-VTe_2, T-VTe_2/graphene/T-VTe_2 and T-VTe_2/graphene/H-VTe_2 sandwiched heterostructures

Sandwiched *T*-VTe_2/graphene/*T*-VTe_2, *H*-VTe_2/graphene/*H*-VTe_2 and *T*-VTe_2/graphene/*H*-VTe_2 heterostructures were designed by deposition of either *T*-VTe_2 or *H*-VTe_2 fragment on top of bilayer *T*-VTe_2/graphene or *H*-VTe_2/graphene heterostructures. Six representative configurations were taken into consideration, namely *H*_gr_*H*_[*AA*], *H*_gr_*H*_[*AB*], *T*_gr_*T*_[*AA′*], *T*_gr_*T*_[*AA*], *T*_gr_*H*_[*AA*] and *T*_gr_*H*_[*AB′*] (Fig. 14). In all triple heterostructures graphene fragment is fixed, and only newly added VTe_2 fragment is moved to create new configurations. "*H*" and "*T*" indicate vanadium ditelluride phases used to construct sandwiches, "gr" is a graphene sheet. Locations of upper VTe_2 fragment relative to bottom VTe_2 fragment are given in square brackets. The label [*AA*] represents sandwiched configurations where *V* atoms of upper VTe_2 fragment are on tops of *V* atoms of bottom VTe_2 fragment and inner *Te* atoms are on the top of outer *Te* atoms. Next configuration with *Te* atoms of upper VTe_2 fragment over *V* atoms of bottom VTe_2 fragment is labeled as [*AB*]. [*AA′*] denotes location *V*, inner *Te* and outer *Te* atoms of upper VTe_2 fragment on tops of *V*, inner *Te* and outer *Te* atoms of bottom VTe_2 fragment, respectively. In [*AB′*] configuration inner *Te* and outer *Te* atoms of upper VTe_2 fragment are over *V* and inner *Te* atoms of bottom VTe_2 fragment, respectively. The *H*_gr_*H*_[*AA*] heterostructure (Fig. 14(*a*)) was constructed by deposition of *H*-VTe_2 monolayer on top of *H*/graphene, so that the stacked configuration demonstrates mirror symmetry relative to graphene layer. Two non-equivalent *C* atoms of graphene fragment is located directly above *V* ($a = 0, b = 0$) and *Te* ($a = 0.(6), b = 0.(3)$) atoms of *H*-VTe_2 fragment. The *H*_gr_*H*_[*AB*] heterostructure (Fig. 14(*b*)) was designed by a shift of upper *H*-VTe_2 layer along diagonal of *a*-*b* plane to $a = 0.(3), b = 0.(6)$. In this heterostructure *Te* atoms of upper *H*-VTe_2 fragment are located directly above *V* atoms of bottom *H*-VTe_2 fragment. Two non-equivalent *C* atoms of graphene fragment are set to sit directly above top of outer and inner *Te* ($a = 0, b = 0$) and *V* ($a = 0.(3), b = 0.(6)$) atoms. The *T*_gr_*T*_[*AA′*] heterostructure (Fig. 14(*c*)) was designed by deposition of *T*-VTe_2 monolayer on top of *T*/graphene with mirror symmetry relative to graphene fragment. Three non-equivalent *C* atoms of graphene fragment are on the tops of *V* ($a = 0, b = 0$), outer *Te* ($a = 0.(3), b = 0.(6)$) and inner *Te* ($a = 0.(6), b = 0.(3)$) atoms of *T*-VTe_2 fragment, respectively. Flipping one *T*-VTe_2 fragment of previous sandwiched heterostructure vertically by 180° leads to *T*_gr_*T*_[*AA*] heterostructure with inversion symmetry, shown in (Fig. 14(*d*)). The flipping of *T*-VTe_2 fragment forms new stacking pattern with graphene: three non-equivalent *C* atoms of graphene are on tops of *V* ($a = 0.(3), b = 0.(6)$), inner *Te* ($a = 0.(3), b = 0.(6)$) and outer *Te* ($a = 0.(6), b = (3)$) atoms, respectively. The *T*_gr_*H*_[*AA*] heterostructure (Fig. 14(*e*)) includes *H* and *T* vanadium ditelluride monolayers, with graphene sitting on the top of VTe_2 fragments being the same as in both *H*- and *T*- bilayer heterostructures. *T*_gr_*H*_[*AB′*] sandwiched heterostructure (Fig. 14(*f*)) was obtained by moving the *H*-VTe_2 layer of previous sandwiched heterostructure to $a = 0.1(6), b = 0.(8)$, so that the inner *Te* atoms of *T*-VTe_2 fragment are located directly above *V* atoms of *H*-VTe_2 fragment. In new stacking pattern non-equivalent *C* atom ($a = 0, b = 0$) is located above hollow site of the *Te*–*V*–*Te* hexagonal ring. Optimization of all initial triple structures with inversion symmetry leads to breakdown of the inversion symmetry due to small structural distortions.

Both parallel (*P*) and antiparallel (*AP*) spin ordering of adjacent ferromagnetic vanadium ditelluride layers were considered for all localized heterostructures. *P* and *AP* imply the same direction of vanadium magnetic moments in each VTe_2 fragment and the same or opposite direction between VTe_2 fragments, respectively. The total magnetic moment of sandwiched heterostructure with *AP* magnetization is equal to zero.

The details of atomic structures of localized triple heterostructures are presented in Fig. 14, Tables 2, and 4. In general, the thicknesses of triple heterostructures are almost the same and varies in the range between 13.67 Å for *T*_gr_*T*_[*AA*] and 14.00 Å for mixed sandwiches. The interlayer distances between graphene and adjacent layers are very close to the interlayer distances for VTe_2/graphene bilayers. Interlayer distances and translation vectors of *H*-VTe_2 based sandwiches are slightly decreased as compared to the same parameters in bilayer *H*/graphene heterostructure while these parameters in *T*-VTe_2 based sandwiches are dependent on the stacking pattern. Because of graphene fragment was already interface matched during optimization with one VTe_2 fragment, atomic positions of the second VTe_2 fragment vary in accordance with new *C* positions, as a result interlayer distances between graphene fragment and first and second VTe_2 fragments are different in some heterostructures. Also magnetic moments on atoms in the first and the second VTe_2 fragments are slightly different. Sandwiches with *P* and *AP* spin ordering have identical structural parameters (translation vectors, heterostructure thicknesses, interlayer distances, bond lengths and values of bond angles) and the same in absolute values magnetic moments on atoms. For this reason, structural parameters and magnetic moments are given only for structures with *P* spin ordering of adjacent layers.

At the PBE level of theory, the values of *C*—*C* and *V*-*Te* bond lengths, *Te*-*V*-*Te* bond angles for all *H*-VTe_2/graphene/*H*-VTe_2 sandwiches are close to corresponding values for *H*/graphene heterostructure. Graphene fragment of the *H*_gr_*H*_[*AA*] is flat whereas graphene fragment of the *H*_gr_*H*_[*AB*] is slightly uneven ($\Delta c = 0.07$ Å). In both configurations magnetic moments on *V*, inner and outer *Te* atoms are

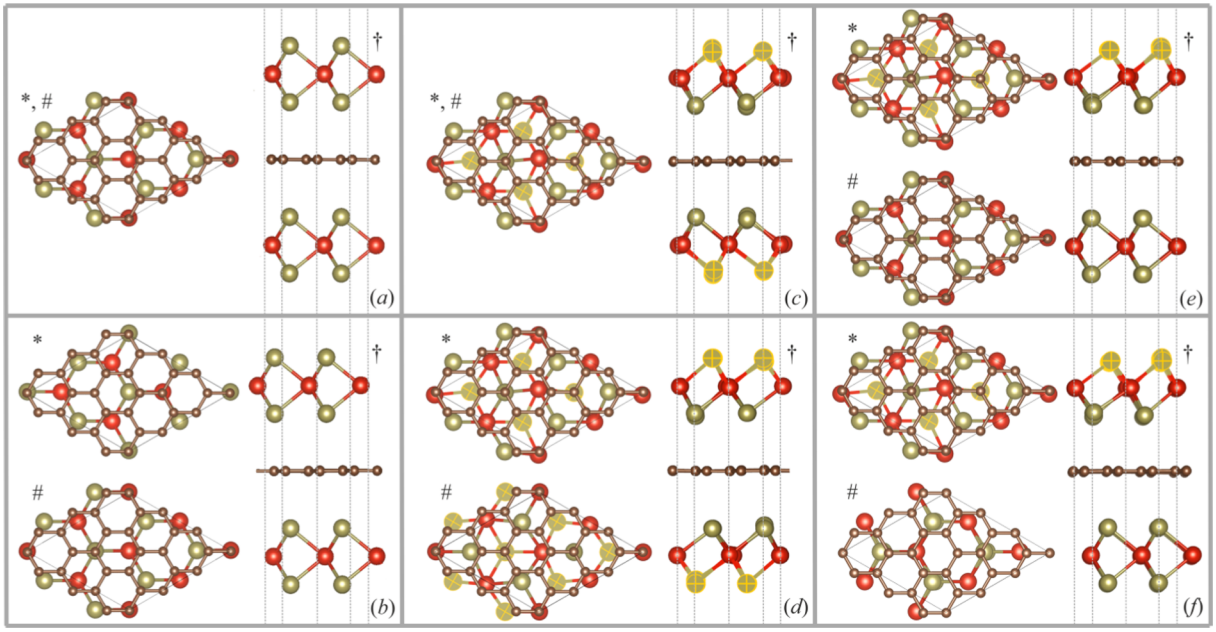

Fig. 14. The atomic structure of six different configurations of localized *H*-VTe_2/graphene/*H*-VTe_2, *T*-VTe_2/graphene/*T*-VTe_2 and *T*-VTe_2/graphene/*H*-VTe_2 heterostructures calculated using PBE functional, namely *H*_gr_*H*_[*AA*] (*a*), *H*_gr_*H*_[*AB*] (*b*), *T*_gr_*T*_[*AA*′] (*c*), *T*_gr_*T*_[*AA*] (*d*), *T*_gr_*H*_[*AA*] (*e*) and *T*_gr_*H*_[*AB*′] (*f*). Here "*H*" and "*T*" indicate vanadium ditelluride phases constructing sandwiches, "gr" is a graphene sheet. Orientation of upper VTe_2 fragment relative to bottom VTe_2 fragment is given in square brackets. [*AA*]: *V* atoms over *V* atoms, inner *Te* atoms over outer *Te* atoms, outer *Te* atoms over inner *Te* atoms; [*AB*]: *Te* atoms over *V* atoms; [*AA*′]: *V* atoms over *V* atoms, inner *Te* atoms over inner *Te* atoms, outer *Te* atoms over outer *Te* atoms; [*AB*′]: inner *Te* atoms over *V* atoms, outer *Te* atoms over inner *Te* atoms. * and #: Top views of the heterostructures in the *a*-*b* plane showing the graphene sitting on the top and bottom VTe_2 fragments, respectively. The same stacking patterns between graphene and both VTe_2 fragments are represented by only one top view and marked *,#. †: Side view of the heterostructures. Red, olive and brown colors correspond to *V*, *Te* and *C* atoms, respectively. *Te* atoms localized far away from graphene sheet are highlighted in yellow. The grey dashed lines are the eye guides for easy comparison of the VTe_2 fragments location relative to each other. (For interpretation of the references to colour in this figure legend, the reader is referred to the web version of this article.)

1.133, −0.086 and −0.088 μ_B, respectively, which are slightly smaller as compared to those in the bilayer heterostructure. The total magnetic moment per unit cell of sandwiched heterostructure is amount to 7.876 μ_B for both configurations.

The distortion of *T*-VTe_2 fragments in *T*-VTe_2/graphene/*T*-VTe_2 and *T*/graphene heterostructures is slightly different. In detail, in *T*_gr_*T*_[*AA*] inner *Te* atoms located directly above *C* atoms are displaced by 0.16 and 0.13 Å towards these carbon atoms compared to others inner *Te* atoms. As a result, neighboring *V* atoms are shifted towards these *Te* atoms, while in bilayer heterostructure *V* atoms are shifted from that *Te* atom to nearest *C* atoms of graphene fragment. *V* (a = 0, b = 0) atoms are also displaced to the graphene plane and located 0.02 Å closer to it compared to other *V* atoms. Two outer *Te* atoms are situated 0.23 and 0.28 Å closer to graphene. The values of the bond lengths are in the same range as in the bilayer heterostructure (Table 4). The maximum difference between carbon atomic positions along *c* axis is 0.09 Å and the *C*—*C* bond length is 1.42 Å. The structure distortion leads to breakdown of the inversion symmetry. Magnetic moments on displaced *V* (a = 0, b = 0) and other *V* atoms are 1.195 and 1.466 μ_B for upper fragment and 1.220 and 1.460 μ_B for bottom one. Magnetic moments on displaced inner and outer *Te* atoms of both *T*-VTe_2 fragments are −0.084 and −0.075 μ_B and on other inner and other outer *Te* atoms are −0.090 and −0.098 μ_B. These values are slightly different as compared to those in *T*/graphene heterostructure. The total magnetic moment of *T*_gr_*T*_[*AA*] unit cell is equal to 9.910 μ_B.

In *T*_gr_*T*_[*AA*′] configuration (Fig. 14(*c*)) *V* atoms located at a = 0.5, b = 0.0 are displaced at 0.04 Å further from graphene plane with magnetic moments equal to 1.220 and 1.240 μ_B, respectively. Observed magnetic moments on other *V* atoms are slightly different and are equal to 1.490, 1.443, 1.478 μ_B in upper *T*-VTe_2 fragment and 1.497, 1.426, 1.487 μ_B in bottom *T*-VTe_2 one. Inner *Te* atoms (a = 0.17, b = 0.34) are displaced towards the shifted *V* atoms and situated at 0.22 or 0.24 Å farther from graphene plane compared with others inner *Te* atoms. The difference in the position of other inner *Te* atoms is small (Δc = 0.06 Å). The outer *Te* atoms (a = 0.84, b = 0.67) are shifted from the *V* atoms, resulting in increasing *V*-*Te* bond lengths. Values of *V*-*Te* bond lengths are in the range from 2.67 to 2.78 Å. (Table 4). The values of magnetic moments on *Te* atoms are in the range from −0.097 to −0.076 μ_B. The total magnetic moment of *T*_gr_*T*_[*AA*′] unit cell is equal to 9.988 μ_B. In this configuration graphene fragment is flat with *C*-*C* bond length is equal to 1.42 Å.

*T*_gr_*H*_[*AA*] and *T*_gr_*H*_[*AB*′] sandwiches are presented in Fig. 14 (*e*) and (*f*), respectively. Structural parameters of *H*-VTe_2 fragment of both configurations are the same as in the bilayer *H*/graphene and threelayer *H*-VTe_2/graphene/*H*-VTe_2 heterostructures. Magnetic moments on *V*, inner and outer *Te* ions of *H*-VTe_2 are 1.133, −0.087 and −0.089 μ_B, respectively, which is very close to those in *H*/graphene and *H*-VTe_2/graphene/*H*-VTe_2. In both configurations the structural distortion of *T*-VTe_2 fragments is practically the same as in *T*_gr_*T*_[*AA*′]. The *V* ion with a = 0.5, b = 0.0 and magnetic moment 1.170 μ_B is located 0.05 Å further from graphene plane. The magnetic moments on other *V* ions are equal to 1.454 μ_B. The inner (a = 0.17, b = 0.34) and outer (a = 0.84, b = 0.67) *Te* ions are located at 0.18 and 0.21 Å further from graphene plane in both configurations with magnetic moments −0.073 and −0.087 μ_B, respectively. The magnetic moments on other inner and outer *Te* ions are equal to −0.093 and −0.090 μ_B. Values of *V*-*Te* bond lengths are in the range from 2.67 to 2.77 Å (Table 4). The maximum difference between carbon atomic positions along *c* axis is 0.02 Å with *C*—*C* bond length equal to 1.41 Å. Total magnetic moments per unit cell of both *T*_gr_*H*_[*AA*] and *T*_gr_*H*_[*AB*′] heterostructures are equal to 8.840 μ_B.

Sandwich structures, formed by two *T*-VTe_2 monolayers and graphene are energetically favorable with the *T*_gr_*T*_[*AA*′] configuration being lowest in energy. The energy difference between *T*-VTe_2/

Table 4
V-Te bond lengths and *Te-V-Te* angles of *T*-VTe_2 fragments of sandwiched heterostructures at the PBE level of theory. The atomic numbering scheme is shown in Fig. 1 (e). Asterisk (*) indicates values for *V* located at $a = 0$ and $b = 0$. All distances are in Å, all angles are in °.

Structure	VTe_2 fragment	Structural parameters								
		Bond	Bond length, Å				Angle	Angle value		
*T*_gr_*T*_[*AA*]	Upper and bottom	2-1	2.77 / 2.76*				2-1-6	171° / 177°*		
		1-6	2.67 / 2.68*				3-1-7	170° / 177°*		
		3-1	2.77 / 2.76*				4-1-5	171° / 177°*		
		1-7	2.67 / 2.68*				2-1-3	83° / 88°*		
		4-1	2.68 / 2.76*				2-1-4	85° / 88°*		
		1-5	2.76 / 2.68*				2-1-5	87° / 95°*		
							2-1-7	95° / 95°*		
							6-1-3	95° / 95°*		
							6-1-4	102° / 95°*		
							6-1-5	85° / 83°*		
							6-1-7	88° / 83°*		
*T*_gr_*T*_[*AA*']	Upper		V ($a = -0.02$, $b = -0.03$)	V ($a = -0.01$, $b = -0.52$)	V ($a = 0.51$, $b = 0.00$)	V ($a = 0.53$, $b = 0.52$)		V ($a = -0.02$, $b = -0.03$)	V ($a = -0.01$, $b = -0.52$)	V ($a = 0.51$, $b = 0.00$)	V ($a = 0.53$, $b = 0.52$)
		2-1	2.68	2.67	2.76	2.78	2-1-6	171°	172°	177°	170°
		1-6	2.76	2.77	2.67	2.68	3-1-7	169°	172°	177°	171°
		3-1	2.69	2.77	2.72	2.69	4-1-5	171°	170°	174°	171°
		1-7	2.75	2.68	2.71	2.75	2-1-3	85°	88°	82°	85°
		4-1	2.78	2.67	2.77	2.67	2-1-4	88°	85°	83°	85°
		1-5	2.68	2.77	2.67	2.76	2-1-5	96°	102°	92°	87°
							2-1-7	103°	94°	95°	86°
							6-1-3	86°	95°	94°	103°
							6-1-4	93°	87°	97°	101°
							6-1-5	82°	85°	88°	86°
							6-1-7	85°	82°	89°	86°
	bottom	2-1	2.69	2.77	2.71	2.69	2-1-6	171°	170°	173°	171°
		1-6	2.74	2.68	2.72	2.74	3-1-7	170°	172°	176°	171°
		3-1	2.78	2.67	2.77	2.67	4-1-5	171°	172°	176°	170°
		1-7	2.68	2.77	2.67	2.76	2-1-3	85°	85°	84°	87°
		4-1	2.67	2.68	2.77	2.78	2-1-4	88°	86°	83°	84°
		1-5	2.77	2.77	2.67	2.67	2-1-5	92°	87°	98°	101°
							2-1-7	101°	87°	98°	92°
							6-1-3	88°	102°	91°	97°
							6-1-4	97°	102°	91°	88°
							6-1-5	83°	85°	87°	86°
							6-1-7	86°	85°	87°	83°
*T*_gr_*H*_[*AA*] and *T*_gr_*H*_[*AB*']	upper	2-1	2.68	2.67	2.75	2.77	2-1-6	171°	171°	177°	170°
		1-6	2.76	2.76	2.68	2.67	3-1-7	169°	171°	177°	171°
		3-1	2.77	2.67	2.75	2.67	4-1-5	171°	170°	176°	171°
		1-7	2.68	2.76	2.68	2.75	2-1-3	85°	88°	83°	85°
		4-1	2.68	2.77	2.74	2.68	2-1-4	88°	85°	83°	85°
		1-5	2.76	2.67	2.69	2.75	2-1-5	95°	102°	94°	87°
							2-1-7	103°	94°	95°	87°
							6-1-3	87°	95°	94°	103°
							6-1-4	94°	87°	95°	102°
							6-1-5	82°	85°	88°	85°
							6-1-7	85°	82°	88°	85°

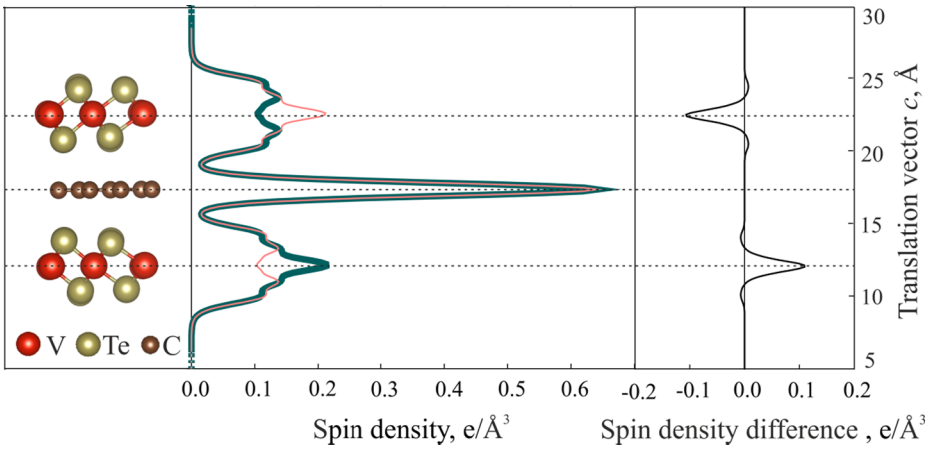

Fig. 15. The atomic structure (left), spin density (middle) and spin density difference ($\rho_\uparrow(r) - \rho_\downarrow(r)$) (right) profiles along the translation vector *c* for energetically favorable sandwich *T*_gr_*T*_[*AA*'] configuration with antiparallel spin ordering of adjacent ferromagnetic *T*-VTe_2 fragments at the PBE level of theory. The translation vector *c* is directed along the thickness of the heterostructure. $\rho_\uparrow(r)$ and $\rho_\downarrow(r)$ are spin densities for electrons with spin-up (↑) and spin-down (↓). Turquoise and pink lines denote up and down spins, respectively. In spin density difference profile (right side of the figure) spin-up and spin-down channels are demonstrated at positive and negative panels, respectively. The horizontal dashed lines are the eye guides for easy comparison the spin density and structure.

graphene/*T*-VTe_2, *T*-VTe_2/graphene/*H*-VTe_2 and *H*-VTe_2/graphene/*H*-VTe_2 is in the range of ~ −0.4/ −0.7 eV (Table 2). The binding energies of all heterostructures are negative. The difference between binding energies of *T*_gr_*T*_[*AA*′] and *T*_gr_*T*_[*AA*] does not exceed 0.003 eV, between binding energies of *T*_gr_*H*_[*AA*] and *T*_gr_*H*_[*AB*′] does not exceed 0.007 eV and between binding energies of *H*_gr_*H*_[*AA*] and *H*_gr_*H*_[*AA*] does not exceed 0.011 eV. All of these values are lower or equal to internal accuracy of DFT approach (1 kJ/mol) and it means that sandwiched heterostructures based on graphene and VTe_2 are insensitive to the stacking ways. The small energy difference between parallel and antiparallel spin orderings points out the possibility of easy magnetic reversal of the spin ordering of upper layer, with the spin ordering of bottom layer remaining unchanged. The MAEs calculations of *T*-VTe_2 fragments for *T*_gr_*T*_[*AA*′] and *T*_gr_*T*_[*AA*] heterostructures indicate that the magnetic easy axis for both heterostructures is oriented along *x* direction like in bilayer *T*/graphene heterostructure with corresponding values of in-plane and out-of-plane MAEs −0.070 and 0.968 meV for *T*_gr_*T*_[*AA*′] and −0.015 and 1.044 meV for *T*_gr_*T*_[*AA*]. These MAEs are slightly larger in absolute values as compared to MAE of bilayer *T*/graphene heterostructure (−0.013 and 0.520 meV, see above).

The electronic structures of energetically favorable sandwiched *T*_gr_*T*_[*AA*′] heterostructure with *AP* spin ordering was studied to verify magnetization of adjacent *T*-VTe_2 fragments. The spin density and spin density difference profiles along *c* axis are presented at Fig. 15. One can see a large predominance of spin-up electron density in one *T*-VTe_2 fragment and spin-down electron density in another one, localized on vanadium atoms at 22.50 and 12.00 Å of the translation vector *c*. The spin densities of opposite signs are localized at *Te* at 24.50, 20.50, 10.00 and 14.00 Å of the translation vector *c*. Spin-up and spin-down densities localized at carbon atoms of graphene are perfectly compensate each other, making graphene spin-neutral fragment.

The partial spin density of states presented at Fig. 16 shows the distribution of spin-up and spin-down densities in upper and bottom *T*-VTe_2 fragments. One can see a large predominance of spin-up or spin-down states at Fermi level and a small amount of states with opposite spins in both fragments. The insert at Fig. 16 shows 1.029 and 6.917 (arb. units) spin-up and 7.516 and 1.267 spin-down partial density of states at the Fermi level in upper and bottom *T*-VTe_2 fragments, respectively (Table 5). Calculated Fermi level spin polarizations are amount to 76 and 69% for the upper and the bottom *T*-VTe_2 fragments,

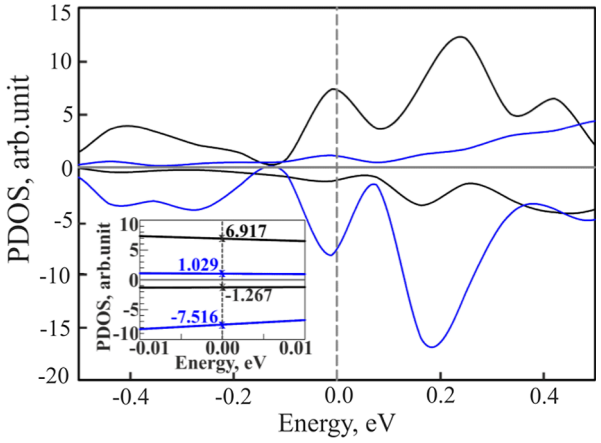

Fig. 16. Partial density of states (PDOSs) for energetically favorable sandwiched *T*_gr_*T*_[*AA*′] heterostructure with antiparallel spin ordering of adjacent ferromagnetic layers at the PBE level of theory. Blue and black lines denote partial density of states of *T*-VTe_2 fragments, located above and below the graphene sheet, respectively. The Fermi level corresponds to zero eV. Spin-up and spin-down channels are demonstrated at upper and bottom panels, respectively. The insert demonstrates PDOSs in the vicinity of the Fermi level. The PDOS values (arbitrary units) at the Fermi level are appropriately marked.

Table 5
Spin-up ($\rho_{\uparrow}(\varepsilon_F)$) and spin-down ($\rho_{\downarrow}(\varepsilon_F)$) partial DOS at the Fermi level and Fermi level spin polarizations (*P*) for *T*-VTe_2 fragments of *T*_gr_*T*_[*AA*′] heterostructure with antiparallel spin ordering of adjacent ferromagnetic layers at PBE level of theory.

Fragment	$\rho_{\uparrow}(\varepsilon_F)$arb. units	$\rho_{\downarrow}(\varepsilon_F)$arb. units	*P*
Upper *T*-VTe_2	1.029	7.516	0.759 (76%)
Bottom *T*-VTe_2	6.917	1.267	0.690 (69%)

respectively. Different polarization ratios for first and second *T*-VTe_2 fragments are caused by nonequivalent binding of VTe_2 monolayers with graphene. The calculated TMR ratio estimated within the Julliere model for *T*_gr_*T*_[*AA*′] heterostructure is equal to 220%, making proposed sandwiched heterostructure a potential candidate to be used as magnetic tunnel junctions for novel spintronic devices operated by tunnelling magnetoresistance or spin transfer torque effects.

4. Conclusions

In summary, new nanoscale bilayer and threelayer vertical heterostructures based on graphene and ferromagnetic vanadium ditelluride monolayers were proposed and atomic and electronic structure and magnetic properties were studied using the state-of-the-art ab initio DFT approach. The results show that graphene has a significant influence on VTe_2 monolayers, resulting in the electron density redistribution in the vicinity of the Fermi level accompanied by significant changes of structural parameters and magnetic moments. In contrast to freestanding monolayer *T*-VTe_2 electronic structure in bilayer *T*/graphene is half-metallic with indirect spin-up band gap of ~0.3 eV, which makes 2D *T*-VTe_2 a promising material for spintronics. The formation of *H*-VTe_2/graphene leads to an increase of band gap of *H*-VTe_2 electronic subsystem and the electronic structure of *H*-VTe_2 monolayer keeps its original semiconductor nature. In both heterostructures graphene fragment is slightly hole doped due to the electron charge transfer to VTe_2 fragment with lifting of the Dirac point up to ~0.2 eV above the Fermi level. The spin splitting of graphene sybsystem in the vicinity of Dirac point was interpreted in terms of exchange splitting. The interlayer distances, binding energies and electron localization functions indicate the van der Waals interaction between the fragments. The bilayer and threelayer heterostructure thicknesses are about of 7 and 14 Å, respectively. All heterostructures are energetically stable. It was shown that electronic subsystems of graphene and VTe_2 monolayers are insensitive to the stacking ways. The small energy difference between parallel and antiparallel spin alignments between the VTe_2 fragments indicates the possibility of easy mutual magnetic reversal of the layers. Heterostructures, formed by *T*-VTe_2 monolayers and graphene are energetically preferred. The *T*-VTe_2 theoretical MAEs have the magnetic easy axis along the *x* direction while freestanding *T*-VTe_2 monolayer has easy *xy* plane of magnetization. It was found that MAEs is to be two orders of magnitude larger than those of Fe and Ni bulks. The *T*_gr_*T*_[*AA*'] sandwich heterostructure is lowest in energy. At the Fermi level the spin-polarization values of VTe_2 fragments are equal to 76 and 69%, respectively, and the TMR ratio estimated within the Julliere model is equal to 220%. Unique electronic and magnetic properties of proposed bi- and trilayered sandwiched vertical heterostrictures open a promising possibility to use the materials as magnetic tunnel junctions for novel spintronic devices.

CRediT authorship contribution statement

Lyudmila V. Begunovich: Investigation, Visualization, Writing - original draft, Writing - review & editing. **Artem V. Kuklin:** Supervision, Resources, Writing - review & editing, Investigation. **Maxim A. Visotin:** Writing - review & editing. **Alexander A. Kuzubov:**

Conceptualization, Methodology. **Felix N. Tomilin:** Project administration. **Anton S. Tarasov:** Writing - original draft, Validation. **Yuri G. Mikhalev:** Supervision, Project administration. **Pavel V. Avramov:** Supervision, Writing - review & editing, Validation.

Declaration of Competing Interest

The authors declare that they have no known competing financial interests or personal relationships that could have appeared to influence the work reported in this paper.

Acknowledgements

This work was supported by the government contract of the Ministry of Science and Higher Education of the Russian Federation to Siberian Federal University (Grant No. 16.1455.2017/PCh) and Russian Foundation for Basic Research, Government of Krasnoyarsk Territory, Krasnoyarsk Regional Fund of Science to the research project: “Quantum chemical modeling of Bychkov-Rashba interfaces based on transition metal compounds and nanoscaled organic fragments”. P.V.A. and A.V.K. gratefully acknowledges the financial support of National Research Foundation of Republic of Korea for support under Grant No. NRF-2017R1A2B4004440. A.V.K. also acknowledges the US Air Force Office of Scientific Research (contract FA-9550-18-1-0032) for support. The authors would like to thank Information Technology Center, Novosibirsk State University, Institute of Computational Modelling of SB RAS, Krasnoyarsk for providing the access to supercomputer facilities, and Irkutsk Supercomputer Center of SB RAS for providing the access to HPC-cluster “Akademik V.M. Matrosov” (Irkutsk Supercomputer Center of SB RAS, Irkutsk: ISDCT SB RAS; http://hpc.icc.ru, accessed 13.05.2019).

References

[1] A. Fert, Origin, development, and future of spintronics (Nobel lecture), Angew. Chemie – Int. Ed. 47 (2008) 5956–5967, https://doi.org/10.1002/anie.200801093.
[2] D.E. Nikonov, I.A. Young, Overview of beyond-CMOS devices and a uniform methodology for their benchmarking, Proc. IEEE 101 (2013) 2498–2533, https://doi.org/10.1109/JPROC.2013.2252317.
[3] M.N. Baibich, J.M. Broto, A. Fert, F. Nguyen Van Dau, F. Petroff, P. Eitenne, G. Creuzet, A. Friederich, J. Chazelas, Giant magnetoresistance of (001)Fe/(001)Cr magnetic superlattices, Phys. Rev. Lett. 61 (1988) 2472–2475, https://doi.org/10.1103/PhysRevLett. 61.2472.
[4] S.S.P. Parkin, C. Kaiser, A. Panchula, P.M. Rice, B. Hughes, M. Samant, S.H. Yang, Giant tunnelling magnetoresistance at room temperature with MgO (100) tunnel barriers, Nat. Mater. 3 (2004) 862–867, https://doi.org/10.1038/nmat1256.
[5] S. Ikeda, J. Hayakawa, Y. Ashizawa, Y.M. Lee, K. Miura, H. Hasegawa, M. Tsunoda, F. Matsukura, H. Ohno, Tunnel magnetoresistance of 604% at 300 K by suppression of Ta diffusion in CoFeB/MgO/CoFeB pseudo-spin-valves annealed at high temperature, Appl. Phys. Lett. 93 (2008) 82508, https://doi.org/10.1063/1.2976435.
[6] Y.M. Lee, J. Hayakawa, S. Ikeda, F. Matsukura, H. Ohno, Giant tunnel magnetoresistance and high annealing stability in CoFeB/MgO/CoFeB magnetic tunnel junctions with synthetic pinned layer, Appl. Phys. Lett. 89 (2006) 42506, https://doi.org/10.1063/1.2234720.
[7] C. Chappert, A. Fert, F.N. Van Dau, The emergence of spin electronics in data storage, Nat. Mater. 6 (2007) 813–823, https://doi.org/10.1038/nmat2024.
[8] J.C. Slonczewski, Current-driven excitation of magnetic multilayers, J. Magn. Magn. Mater. 159 (1996) L1–L7, https://doi.org/10.1016/0304-8853(96)00062-5.
[9] L. Thomas, G. Jan, J. Zhu, H. Liu, Y.J. Lee, S. Le, R.-Y. Tong, K. Pi, Y.-J. Wang, D. Shen, R. He, J. Haq, J. Teng, V. Lam, K. Huang, T. Zhong, T. Torng, P.-K. Wang, Perpendicular spin transfer torque magnetic random access memories with high spin torque efficiency and thermal stability for embedded applications (invited), J. Appl. Phys. 115 (2014) 17261, https://doi.org/10.1063/1.4870917.
[10] A.A. Tulapurkar, Y. Suzuki, A. Fukushima, H. Kubota, H. Maehara, K. Tsunekawa, D.D. Djayaprawira, N. Watanabe, S. Yuasa, Spin-torque diode effect in magnetic tunnel junctions, Nature 438 (2005) 339–342, https://doi.org/10.1038/nature04207.
[11] J. Grollier, D. Querlioz, M.D. Stiles, Spintronic Nanodevices for Bioinspired Computing, Proc. IEEE 104 (2016) 2024–2039, https://doi.org/10.1109/JPROC.2016.2597152.
[12] S. Bhatti, R. Sbiaa, A. Hirohata, H. Ohno, S. Fukami, S.N. Piramanayagam, Spintronics based random access memory: a review, Mater. Today 20 (2017) 530–548, https://doi.org/10.1016/j.mattod.2017.07.007.
[13] W. Yan, O. Txoperena, R. Llopis, H. Dery, L.E. Hueso, F. Casanova, A two-dimensional spin field-effect switch, Nat. Commun. 7 (2016) 13372, https://doi.org/10.1038/ncomms13372.
[14] A. Dankert, S.P. Dash, Electrical gate control of spin current in van der Waals heterostructures at room temperature, Nat. Commun. 8 (2017) 16093, https://doi.org/10.1038/ncomms16093.
[15] C. Tan, Z. Liu, W. Huang, H. Zhang, Non-volatile resistive memory devices based on solution-processed ultrathin two-dimensional nanomaterials, Chem. Soc. Rev. 44 (2015) 2615–2628, https://doi.org/10.1039/C4CS00399C.
[16] R. Lv, J.A. Robinson, R.E. Schaak, D. Sun, Y. Sun, T.E. Mallouk, M. Terrones, Transition metal dichalcogenides and beyond: synthesis, properties, and applications of single- and few-layer nanosheets, Acc. Chem. Res. 48 (2015) 56–64, https://doi.org/10.1021/ar5002846.
[17] D. Yoo, M. Kim, S. Jeong, J. Han, J. Cheon, Chemical synthetic strategy for single-layer transition-metal chalcogenides, J. Am. Chem. Soc. 42 (2014) 14670–14673, https://doi.org/10.1021/ja5079943.
[18] J. Feng, X. Sun, C. Wu, L. Peng, C. Lin, S. Hu, J. Yang, Y. Xie, Metallic few-layered VS_2 ultrathin nanosheets: high two-dimensional conductivity for in-plane supercapacitors, J. Am. Chem. Soc. 133 (2011) 17832–17838, https://doi.org/10.1021/ja207176c.
[19] Q.H. Wang, K. Kalantar-Zadeh, A. Kis, J.N. Coleman, M.S. Strano, Electronics and optoelectronics of two-dimensional transition metal dichalcogenides, Nat. Nanotechnol. 7 (2012) 699–712, https://doi.org/10.1038/nnano.2012.193.
[20] G. Eda, H. Yamaguchi, D. Voiry, T. Fujita, M. Chen, M. Chhowalla, Photoluminescence from chemically exfoliated MoS_2, Nano Lett. 11 (2011) 699–712, https://doi.org/10.1021/nl201874w.
[21] J.N. Coleman, M. Lotya, A. O’Neill, S.D. Bergin, P.J. King, U. Khan, K. Young, A. Gaucher, S. De, R.J. Smith, I.V. Shvets, S.K. Arora, G. Stanton, H.-Y. Kim, K. Lee, G.T. Kim, G.S. Duesberg, T. Hallam, J.J. Boland, J.J. Wang, J.F. Donegan, J.C. Grunlan, G. Moriarty, A. Shmeliov, R.J. Nicholls, J.M. Perkins, E.M. Grieveson, K. Theuwissen, D.W. McComb, P.D. Nellist, V. Nicolosi, Two-dimensional nanosheets produced by liquid exfoliation of layered materials, Science 331 (2011) 568–571, https://doi.org/10.1126/science.1194975.
[22] Y. Shi, H. Li, L.J. Li, Recent advances in controlled synthesis of two-dimensional transition metal dichalcogenides *via* vapour deposition techniques, Chem. Soc. Rev. 44 (2015) 2744–2756, https://doi.org/10.1039/c4cs00256c.
[23] J. Zhou, J. Lin, X. Huang, Y. Zhou, Y. Chen, J. Xia, H. Wang, Y. Xie, H. Yu, J. Lei, D. Wu, F. Liu, Q. Fu, Q. Zeng, C.-H. Hsu, C. Yang, L. Lu, T. Yu, Z. Shen, H. Lin, B.I. Yakobson, Q. Liu, K. Suenaga, G. Liu, Z. Liu, A library of atomically thin metal chalcogenides, Nature 556 (2018) 355–359, https://doi.org/10.1038/s41586-018-0008-3.
[24] A.H.M.A. Wasey, S. Chakrabarty, G.P. Das, Quantum size effects in layered VX_2(X = S, Se) materials: manifestation of metal to semimetal or semiconductor transition, J. Appl. Phys. 117 (2015) 64313, https://doi.org/10.1063/1.4908114.
[25] H. Pan, Electronic and magnetic properties of vanadium dichalcogenides monolayers tuned by hydrogenation, J. Phys. Chem. C 118 (2014) 13248–13253, https://doi.org/10.1021/jp503030b.
[26] H.-R. Fuh, C.-R. Chang, Y.-K. Wang, R.F.L. Evans, R.W. Chantrell, H.-T. Jeng, Newtype single-layer magnetic semiconductor in transition-metal dichalcogenides VX_2 (X = S, Se and Te), Sci. Rep. 6 (2016) 32625, https://doi.org/10.1038/srep32625.
[27] Y. Ma, Y. Dai, M. Guo, C. Niu, Y. Zhu, B. Huang, Evidence of the existence of magnetism in pristine VX_2 monolayers (X = S, Se) and their strain-induced tunable magnetic properties, ACS Nano 6 (2012) 1695–1701, https://doi.org/10.1021/nn204667z.
[28] I. Vatansever, S. Sarikurt, R.F.L. Evans, Hysteresis features of the transition-metal dichalcogenides VX_2 (X = S, Se, and Te), Mater. Res. Express 5 (2018) 46108, https://doi.org/10.1088/2053-1591/aabca6.
[29] D. Gao, Q. Xue, X. Mao, W. Wang, Q. Xu, D. Xue, Ferromagnetism in ultrathin VS_2 nanosheets, J. Mater. Chem. C 1 (2013) 5909–5916, https://doi.org/10.1039/C3tc31233j.
[30] M. Bonilla, S. Kolekar, Y. Ma, H.C. Diaz, V. Kalappattil, R. Das, T. Eggers, H.R. Gutierrez, M.-H. Phan, M. Batzill, Strong room-temperature ferromagnetism in VSe_2 monolayers on van der Waals substrates, Nat. Nanotechnol. 13 (2018) 289–293, https://doi.org/10.1038/s41565-018-0063-9.
[31] J. Li, B. Zhao, P. Chen, R. Wu, B. Li, Q. Xia, G. Guo, J. Luo, K. Zang, Z. Zhang, H. Ma, G. Sun, X. Duan, X. Duan, Synthesis of ultrathin metallic MTe_2(M = V, Nb, Ta) single-crystalline nanoplates, Adv. Mater. 30 (2018) 1801043, https://doi.org/10.1002/adma.201801043.
[32] A.V. Kuklin, S.A. Shostak, A.A. Kuzubov, Two-dimensional lattices of VN: emergence of ferromagnetism and half-metallicity on nanoscale, J. Phys. Chem. Lett. 9 (2018) 1422–1428, https://doi.org/10.1021/acs.jpclett.7b03276.
[33] J. Hu, B. Xu, C. Ouyang, S.A. Yang, Y. Yao, Investigations on V_2C and V_2CX_2 (X = F, OH) monolayer as a promising anode material for Li ion batteries from first-principles calculations, J. Phys. Chem. C 118 (2014) 24274–24281, https://doi.org/10.1021/jp507336x.
[34] J. He, S. Ma, P. Lyu, P. Nachtigall, Unusual Dirac half-metallicity with intrinsic ferromagnetism in vanadium trihalide monolayers, J. Mater. Chem. C 4 (2016) 2518–2526, https://doi.org/10.1039/C6TC00409A.
[35] C. Ataca, H. Şahin, S. Ciraci, Stable, single-layer MX_2 transition-metal oxides and dichalcogenides in a honeycomb-like structure, J. Phys. Chem. C 116 (2012) 8983–8999, https://doi.org/10.1021/jp212558p.
[36] Z.I. Popov, N.S. Mikhaleva, M.A. Visotin, A.A. Kuzubov, S. Entani, H. Naramoto, S. Sakai, P.B. Sorokin, P.V. Avramov, The electronic structure and spin states of 2D graphene/VX_2 (X = S, Se) heterostructures, Phys. Chem. Chem. Phys. 18 (2016) 33047–33052, https://doi.org/10.1039/C6CP06732H.
[37] X. Yuan, M. Yang, L. Wang, Y. Li, Structural stability and intriguing electronic properties of two-dimensional transition metal dichalcogenide alloys, Phys. Chem.

Chem. Phys. 19 (2017) 13846–13854, https://doi.org/10.1039/C7CP01727H.
[38] M. Chhowalla, H.S. Shin, G. Eda, L.-J. Li, K.P. Loh, H. Zhang, The chemistry of two-dimensional layered transition metal dichalcogenide nanosheets, Nat. Chem. 5 (2013) 263–275, https://doi.org/10.1038/nchem.1589.
[39] H. Pan, Metal dichalcogenides monolayers: novel catalysts for electrochemical hydrogen production, Sci. Rep. 4 (2014) 5348, https://doi.org/10.1038/srep05348.
[40] K. Xu, P. Chen, X. Li, C. Wu, Y. Guo, J. Zhao, X. Wu, Y. Xie, Ultrathin nanosheets of vanadium diselenide: a metallic two-dimensional material with ferromagnetic charge-density-wave behavior, Angew. Chemie - Int. Ed. 52 (2013) 10477–10481, https://doi.org/10.1002/anie.201304337.
[41] X. Xu, W. Yao, D. Xiao, T.F. Heinz, Spin and pseudospins in transition metal dichalcogenides, Nat. Phys. 10 (2014) 343–350, https://doi.org/10.1109/SUM.2014.8.
[42] N. Lu, H. Guo, L. Li, J. Dai, L. Wang, W.-N. Mei, X. Wu, X.C. Zeng, MoS_2/MX_2 heterobilayers: bandgap engineering via tensile strain or external electrical field, Nanoscale. 6 (2014) 2879–2886, https://doi.org/10.1039/c3nr06072a.
[43] W. Han, R.K. Kawakami, M. Gmitra, J. Fabian, Graphene spintronics, Nat. Nanotechnol. 9 (2014) 794–807, https://doi.org/10.1038/nnano.2014.214.
[44] Enrique Cobas, Adam L. Friedman, Olaf M.J. van't Erve, Jeremy T. Robinson, Berend T. Jonker, Graphene as a tunnel barrier: graphene-based magnetic tunnel junctions, Nano Lett. 12 (6) (2012) 3000–3004, https://doi.org/10.1021/nl3007616.
[45] W. Fang, H. Zhao, Y. Xie, J. Fang, J. Xu, Z. Chen, Facile hydrothermal synthesis of VS_2/graphene nanocomposites with superior high-rate capability as lithium-ion battery cathodes, ACS Appl. Mater. Interfaces 7 (2015) 13044–13052, https://doi.org/10.1021/acsami.5b03124.
[46] B. Cho, J. Yoon, S.K. Lim, A.R. Kim, D.H. Kim, S.-G. Park, J.-D. Kwon, Y.-J. Lee, K.-H. Lee, B.H. Lee, H.C. Ko, M.G. Hahm, Chemical sensing of 2D graphene/MoS_2 heterostructure device, ACS Appl. Mater. Interfaces 7 (2015) 16775–16780, https://doi.org/10.1021/acsami.5b04541.
[47] J.P. Perdew, K. Burke, M. Ernzerhof, Generalized gradient approximation made simple, Phys. Rev. Lett. 77 (1996) 3865–3868, https://doi.org/10.1103/PhysRevLett.77.3865.
[48] G. Kresse, J. Furthmuller, Efficient iterative schemes for ab initio total-energy calculations using a plane-wave basis set, Phys. Rev. B. 54 (1996) 11169–11186.
[49] S. Grimme, Semiempirical GGA-type density functional constructed with a long-range dispersion correction, J. Comput. Chem. 27 (2006) 1787, https://doi.org/10.1002/jcc.
[50] P.E. Bloch, Projector augmented-wave method, Phys. Rev. B. 50 (1994) 17953–17979.
[51] H.J. Monkhorst, J.D. Pack, Special points for Brillouin-zone integrations, Phys. Rev. B. 13 (1976) 5188–5192.
[52] A.V. Krukau, O.A. Vydrov, A.F. Izmaylov, G.E. Scuseria, Influence of the exchange screening parameter on the performance of screened hybrid functionals, J. Chem. Phys. 125 (2006) 224106, https://doi.org/10.1063/1.2404663.
[53] K. Momma, F. Izumi, VESTA 3 for three-dimensional visualization of crystal, volumetric and morphology data, J. Appl. Crystallogr. 44 (2011) 1272–1276, https://doi.org/10.1107/S0021889811038970.
[54] E. van Lenthe, E.J. Baerends, J.G. Snijders, Relativistic regular two-component hamiltonians, J. Chem. Phys. 99 (1993) 4597–4610, https://doi.org/10.1063/1.466059.
[55] D. Hobbs, G. Kresse, J. Hafner, Fully unconstrained noncollinear magnetism within the projector augmented-wave method, Phys. Rev. B. 62 (2000) 11556–11570, https://doi.org/10.1103/PhysRevB.62.11556.
[56] S. Steiner, S. Khmelevskyi, M. Marsmann, G. Kresse, Calculation of the magnetic anisotropy with projected-augmented-wave methodology and the case study of disordered $Fe_{1-x}Co_x$ alloys, Phys. Rev. B. 93 (2016) 224425, https://doi.org/10.1103/PhysRevB.93.224425.
[57] M. Julliere, Tunneling between ferromagnetic films, Phys. Lett. A 54 (1975) 225–226, https://doi.org/10.1016/0375-9601(75)90174-7.
[58] N.V. Volkov, Spintronics: manganite-based magnetic tunnel structures, Uspekhi Fiz. Nauk. 55 (2012) 250–269, https://doi.org/10.3367/UFNe.0182.201203b.0263.
[59] I. Yang, S.Y. Savrasov, G. Kotliar, Importance of correlation effects on magnetic anisotropy in Fe and Ni, Phys. Rev. Lett. 87 (2001) 216405, https://doi.org/10.1103/PhysRevLett.87.216405.
[60] C. Zhang, C. Gong, Y. Nie, K.-A. Min, C. Liang, Y.J. Oh, H. Zhang, W. Wang, S. Hong, L. Colombo, R.M. Wallace, K. Cho, Systematic study of electronic structure and band alignment of monolayer transition metal dichalcogenides in Van der Waals heterostructures, 2D Mater. 4 (2017) 015026. doi:10.1088/2053-1583/4/1/015026.
[61] A. Chanana, S. Mahapatra, Prospects of zero Schottky barrier height in a graphene-inserted MoS_2-metal interface, J. Appl. Phys. 119 (2016) 14303, https://doi.org/10.1063/1.4938742.
[62] X. Zhang, Q. Liu, J.-W. Luo, A.J. Freeman, A. Zunger, Hidden spin polarization in inversion-symmetric bulk crystals, Nat. Phys. 10 (2014) 387–393, https://doi.org/10.1038/nphys2933.
[63] E.I. Rashba, Properties of semiconductors with an extremum loop .1. Cyclotron and combinational resonance in a magnetic field perpendicular to the plane of the loop, Sov. Phys.-Solid State. 2 (1960) 1109–1122. doi:citeulike-article-id:3433984.
[64] M. Gmitra, S. Konschuh, C. Ertler, C. Ambrosch-Draxl, J. Fabian, Band-structure topologies of graphene: Spin-orbit coupling effects from first principles, Phys. Rev. B. 80 (2009) 235431, https://doi.org/10.1103/PhysRevB.80.235431.
[65] S. Abdelouahed, A. Ernst, J. Henk, I.V. Maznichenko, I. Mertig, Spin-split electronic states in graphene: Effects due to lattice deformation, Rashba effect, and adatoms by first principles, Phys. Rev. 82 (2010) 125424, https://doi.org/10.1103/PhysRevB.82.125424.
[66] O. Rader, A. Varykhalov, J. Sánchez-Barriga, D. Marchenko, A. Rybkin, A.M. Shikin, Is there a Rashba effect in graphene on 3d ferromagnets? Phys. Rev. Lett. 102 (2009) 57602, https://doi.org/10.1103/PhysRevLett. 102.057602.
[67] B. Silvi, A. Savin, Classification of chemical bonds on topological analysis of electron localization functions, Lett. Nat. 371 (1994) 683, https://doi.org/10.1038/371683a0.